Title	Application of remote sensing for characterization of windthrow and landslides at multiple scales in forest landscape
Author(s)	Furukawa, Flavio
Degree Grantor	北海道大学
Degree Name	博士(農学)
Dissertation Number	甲第15153号
Issue Date	2022-09-26
DOI	https://doi.org/10.14943/doctoral.k15153
Doc URL	https://hdl.handle.net/2115/87235
Type	doctoral thesis
File Information	Flavio_Furukawa.pdf

Application of remote sensing for characterization of windthrow and landslides at multiple scales in forest landscape

（マルチスケールでの風倒地・崩壊地の特性把握―森林景観におけるリモートセンシングの応用―）

北海道大学 大学院農学院
先進農学フロンティア特別コース　博士後期課程

Flavio Furukawa

TABLE OF CONTENTS

ABSTRACT 3

CHAPTER 1: INTRODUCTION 5

CHAPTER 2: COMPARISON OF CONVENTIONAL CHANGE DETECTION METHODOLOGIES USING HIGH-RESOLUTION IMAGERY TO FIND FOREST DAMAGE CAUSED BY TYPHOONS 11

CHAPTER 3: COMPARISON OF RGB AND MULTISPECTRAL UAV FOR MONITORING VEGETATION COVERAGE CHANGES ON A LANDSLIDE AREA 42

CHAPTER 4: UAV VIDEO-BASED APPROACH TO IDENTIFY DAMAGED TREES IN A WINDTHROW AREA 65

CHAPTER 5: GENERAL DISCUSSIONS 89

APPENDIX 95

ACKNOWLEDGMENTS 97

REFERENCES 99

ABSTRACT

Due to climate change, the frequency, size, and intensity of natural disturbances are increasing, leading to increase damage to forest ecosystems. Proper management of these disturbed areas is critical for the resilience of forest ecosystems. Remote sensing is used for monitoring different stages of disaster management as it can provide essential information about damaged areas, reducing the need for manual inspection of hazardous sites. However, remote sensing has some challenges, such as the influence of elements like atmosphere, clouds, topography, and sun position, generating noise in the output data. The remote sensing community is addressing these challenges and developing new techniques to improve scientific understanding. Still, there is a discrepancy between technical development and application of remote sensing in the management of forest landscapes, due to the need for interdisciplinary skills involved. Since quick and accessible information on disturbed areas is critical, appropriate approaches according to the scale are required to support forest managers.

In this thesis, three different approaches were proposed to facilitate the implementation of remote sensing to characterize windthrow and landslides at three different scales: regional scale, forest stand scale, and single tree scale. The first approach (Chapter 2) compared three different classification methods using high temporal/ spatial resolution satellite data: the normalized difference vegetation index (NDVI) filtering method, spectral angle mapper (SAM) method, and support vector machine (SVM) method. The results showed that the NDVI filtering method was better to identify landslides, while the SAM method was better to identify windthrow; supporting forest managers to choose appropriate methods to identify windthrow and landslides.

The second approach (Chapter 3) compared a Red Green Blue (RGB) unmanned aerial vehicle (UAV) with a Multispectral UAV to characterize landslides throughout the months at a forest stand scale. The results showed that the RGB UAV was able only to monitor vegetation growth, while the Multispectral UAV, due to the higher spectral resolution, could monitor vegetation, bare soil, and dead matter over the months. Both systems, due to the high spatial and temporal resolution, were able to deliver an understanding of the vegetation regeneration process in a landslide at a forest stand scale. The third approach (Chapter 4) was based on full motion video (FMV) technology to identify fallen and snapped trees, at a single tree scale. The results showed that FMV was able to identify fallen and snapped trees in a windthrow area, even with the presence of vegetation. The higher context-awareness provided by the video and simpler workflow showed the potential to overcome the limitations of the UAV structure from motion (SfM) photogrammetry process.

In conclusion, the study examined different approaches on three different scales for the use of remote sensing in the management of disturbed forest areas. As climate change advances, the need to take quick actions to mitigate and sustain resilience in forest ecosystems is essential. Remote sensing will continue to develop and play an important role in forest management after natural disturbances. However, more research needs to be conducted on facilitating the implementation of remote sensing techniques and training forest managers to take full advantage of remote sensing for forest management after natural disturbances.

CHAPTER 1: INTRODUCTION

1.1 Increase of Natural Disturbances in Forest Ecosystems

Forest ecosystems are usually disturbed by wind storms, floods, earthquakes, fires, and volcanic eruptions (Duncan, 1993; Heinselman, 1973; Turner et al., 1997; Veblen et al., 1992). One of the main natural disturbances affecting forest ecosystems in eastern Asia is typhoons (Yamamoto, 1989), mainly due to strong winds and heavy rains (Dale et al., 2001; Mabry et al., 1998). According to projections under the Intergovernmental Panel on Climate Change (IPCC) A1B scenario showed that the frequency of intense tropical cyclones is expected to increase by the end of the twenty-first century (Murakami et al., 2012). As disturbances increase in frequency, size, and strength, the probability of forest stands being affected also increases (Kulakowski et al., 2017). According to Seidl et al. (2017), these disturbances have great potential to impact the ecosystem services provided by forests, and may also exceed the ecological resilience of forest ecosystems.

The understanding and proper management of disturbed forest ecosystems are important to sustain and recover forest service functions (Kulakowski et al., 2017; Morimoto & Negishi, 2019; Thompson et al., 2009; Waldron et al., 2013). While some studies emphasized the importance of salvage logging to control insect outbreaks and forest fire (Dobor et al., 2020; Leduc et al., 2015; Leverkus et al., 2021), other studies emphasized the ecological importance of the deadwood (Cooper-Ellis et al., 1999; Mori et al., 2017; Morimoto et al., 2019; Siitonen, 2001). The identification and characterization of forest disturbed areas are critical in recognizing proper management measures to improve forest resilience (Thompson et al., 2009; Waldron et al., 2013).

1.2 Remote Sensing for Forest Management After Natural Disturbances

Remote sensing is a widely used technology to monitor different stages of disaster management (Boccardo & Giulio Tonolo, 2015; Joyce, Belliss, et al., 2009; Van Westen, 2000), delivering quick and relevant information to support planners, scientists, and decision-makers (Rozenstein & Karnieli, 2011; Rwanga & Ndambuki, 2017). The remote sensing technology allows the gathering of detailed information to understand changes in landcover, drought monitoring, and analysis of complex attributes over space and time (Blaschke, 2010; Hansen & Loveland, 2012; Langner et al., 2012; West et al., 2019). Different types of sensors onboard satellites, airborne, or UAVs can deliver information at different scales, which is an important factor in extracting appropriate data (Woodcock & Strahler, 1987). Combined with different methods of classification and analysis, remote sensing offers important information to define strategies for the management of disturbed forest areas.

As quick information is key to providing essential intelligence to emergency services and decision-makers in a timely manner (Joyce et al., 2009), the advancement in the availability of satellite datasets and processing platforms (European Space Agency, 2022; Gorelick et al., 2017), allowed the identification of disturbed areas (Chiang et al., 2014), assessment of vegetation recovery (Lin et al., 2004), characterization of affected areas (Hervás et al., 2003), and creation of historical datasets (Martha et al., 2012) to understand changes following natural disturbances.

UAVs are also playing an important role in better understanding disturbed areas, and overcoming some of the limitations of satellite-based remote sensing, such as low spatial resolution and the little flexibility in acquisition features, i.e. cloud cover, view angle, and acquisition time (Alvarez-Vanhard et al., 2021). Several studies showed the usage of UAVs to characterize disturbed forest areas (Lazzeri et al., 2021; Lucieer et al., 2014). Furthermore, the intensive development in technology, data availability, and accessibility are also supporting the increased usage of remote sensing by non-experts (Chasmer et al., 2022; Gülch et al., 2012)

1.3 The Challenges of Remote Sensing for Forest Management After Natural Disturbances

Passive optical remote sensing - when the sensor detects natural energy that is emitted or reflected by the observed material - is widely used for forestry, because of data availability and cost-effectiveness (Kangas & Maltamo, 2006). To use those datasets, preprocessing is essential to reduce noise and increase the interpretability of the imagery. This is particularly necessary when using imagery from different sources, or for time series analysis (Xie et al., 2008), as the images should appear as if they were acquired from the same sensor (Hall et al., 1991). Satellite imagery analysis usually contains uncertainty (Song & Woodcock, 2003), due to the influence of elements such as atmosphere, clouds, topography, and sun position (Jianyaa et al., 2008; Song & Woodcock, 2003). For lower spatial resolution satellites, mixels (where one pixel contains multiple land cover categories) are also a challenge to properly classify imagery (Okamoto & Fukuhara, 1996; D. Wang et al., 2009).

For UAV remote sensing, a technology that is commonly used is the structure from motion (SfM) photogrammetry (Carvajal-Ramírez et al., 2021), where a sequence of images is taken and processed to create orthomosaics and three-dimension point clouds

(Iglhaut et al., 2019). The fundamental principle of SfM photogrammetry is also based on passive optical data, being susceptible to illumination conditions, affecting the output of the SfM photogrammetry (Berra & Peppa, 2020; Duffy et al., 2018; Rothmund et al., 2017). Compared with satellite multispectral sensors, UAV sensors usually deliver less homogenous spectral response datasets. This occurs due to the smaller number of bands and the nature of the sensor, which can generate noise that leads to uncertainty in image classification (Coburn et al., 2018; Messina & Modica, 2020). The remote sensing community is still developing the technology to overcome these limitations and take advantage of the variety of datasets and methodologies available today to advance scientific understanding (Giri, 2016). On the other hand, there is a disparity between remote sensing research and its usage (Schweik & Thomas, 2002), mainly due to the necessity of interdisciplinary skills to link research and practice (Bernd et al., 2017; Chasmer et al., 2022). Today, there is high availability of data and methods to preprocess and process remotely sensed data, but no super classifier can be used for all applications (Xie et al., 2008). As quick information is key for disaster management (Joyce et al., 2009), appropriate approaches (methods and/or tools) according to the scale are required to support forest managers in using remote sensing technology for forest management after natural disturbances.

1.4 The Aim of the Thesis

The goal of this thesis was to propose three different approaches to facilitate the implementation of remote sensing to characterize windthrow and landslides at multiple scales. This thesis covers from finding windthrow and landslide areas at a regional scale to monitoring vegetation recovery in landslide areas (forest stand scale), and identification of types of damage on trees within a windthrow area (single tree scale). To address the objectives, in Chapter 2, three different conventional remote sensing techniques were compared, the NDVI filtering method, the SAM method, and the SVM method, to identify windthrow and landslides in Hokkaido, Japan, using high spatial/ temporal resolution satellite imagery.

Concerning the monitoring of landslide areas, in Chapter 3, two different UAVs – one with a multispectral sensor and another with an RGB sensor – were compared to evaluate how these low-cost technologies can support the characterization of a landslide area to monitor vegetation recovery over the months. In addition to this, a methodology based on a video taken from a UAV combined with GIS was proposed to identify fallen and snapped trees in a windthrow area to determine how this approach could support the implementation of remote sensing to characterize windthrow areas in Chapter 4.

CHAPTER 2: COMPARISON OF CONVENTIONAL CHANGE DETECTION METHODOLOGIES USING HIGH-RESOLUTION IMAGERY TO FIND FOREST DAMAGE CAUSED BY TYPHOONS

2.1 Abstract

The number of intense tropical cyclones is expected to increase in the future, causing severe damage to forest ecosystems. Remote sensing plays an important role in detecting changes in land cover caused by tropical storms. Remote sensing techniques have been widely used in different phases of disaster management because they can deliver information quickly to the concerned parties. Although remote sensing technology is already available, an examination of appropriate methods according to the type of damage is still missing. Our goal is to compare the suitability of three different conventional classification methods for quick and easy change detection analysis using high-spatial-resolution and high-temporal-resolution remote sensing imagery to identify areas with windthrow and landslides caused by typhoons. In August 2016, four typhoons hit Hokkaido, the northern island of Japan, and created large areas of windthrow and landslides. I compared the normalized difference vegetation index filtering method, the spectral angle mapper method, and the support vector machine method to identify windthrow and landslides in two study sites in southwestern Hokkaido. These methodologies were evaluated using Planetscope data with a resolution of 3 m/px and validated with reference data based on Worldview2 data with a very high resolution of 0.46 m/px. The results showed that all three methods, when applied to high-spatial-resolution imagery, can yield sufficient results for windthrow and landslide detection. In particular, the spectral angle mapper method performed better at windthrow detection, and the normalized difference vegetation index filtering method performed better at landslide detection.

Keywords: windthrow; landslide; remote sensing; change detection; NDVI filtering; spectral angle mapper, support vector machine; planetscope

2.2 Introduction

The projections under the Intergovernmental Panel on Climate Change (IPCC) A1B scenario showed that there will be a decrease in the number of tropical cyclones globally due to climate change, but the frequency of intense tropical cyclones is expected to increase by the end of the twenty-first century (Murakami et al., 2012), leading to an increase in windthrow and landslide disturbances affecting forest ecosystems.

Remote sensing is a technology that is widely used in different phases of disaster management (Boccardo & Giulio Tonolo, 2015; Van Westen, 2000) quickly delivering information to support planners, scientists, and decision-makers (Rozenstein & Karnieli, 2011; Rwanga & Ndambuki, 2017). Automatic classification of remotely sensed data is suitable for identifying land cover changes, with some caveats, such as the limited pattern recognition ability compared to that of the human brain (Klemas, 2009). Apart from an automatic classification process, the quality of input data is of extreme importance for change detection analysis. If the temporal resolution is low, it may not be possible to check the effects of certain natural disturbances on land cover (Joyce et al., 2009). In contrast, higher-spatial-resolution images also reduce the occurrence of mixels (Okamoto & Fukuhara, 1996), improving the identification of damages in the final result.

The remote sensing community has also contributed to the evolution of this application by developing more accurate and efficient change detection techniques, such as deep learning using very-high-resolution images (Hamdi et al., 2019), UAVs for mapping (Mokroš et al., 2017), and post-classification methods to improve accuracy (C. Wu et al., 2017). Although all these technologies are available, an examination of appropriate methods for quick and reliable land cover change detection depending on the type of damage is still missing (Einzmann et al., 2017). The evolution of remote sensing has made this technology accessible to a broader range of end-users (Kupfer & Emerson, 2005; J. Wang et al., 2014), but skill levels to apply complex algorithms for change detection are still insufficient.

In 2016, four typhoons hit the island of Hokkaido, Japan, damaging a total of 9,000 ha of forest and triggering two major types of damage: windthrow and landslides (Forest Management Division, Bureau of Forestry, Department of Fisheries and Forestry, 2018). Images taken before and after the arrival of the typhoons were used to compare the suitability of three different conventional change detection methodologies to identify windthrow and landslide damage: the NDVI filtering method, the SAM method, and the SVM method. This study selected Planetscope imagery with high spatial and temporal resolutions to ensure the reliability of the change detection analysis (Olofsson et al., 2013).

The methodologies were chosen based on their relative operational simplicity, fast processing, and satisfactory results in previous studies. The NDVI filtering method, presented in Tsai et al. (2011), was used to preliminarily identify landslides and was able to effectively detect landslides in combination with change vector analysis. For windthrow detection, the SAM classifier was considered fast and relatively easy to apply, yielding satisfactory results in combination with multivariate alteration detection postprocessing (Einzmann et al., 2017). The SVM method, although more sophisticated than the other methods, is implemented as part of the Google Earth Engine platform, which makes it easy to apply, and through cloud computing delivering fast results (Gorelick et al., 2017).

Therefore, the goal of this chapter was to compare the suitability of three conventional remote sensing methods when used separately for quick and easy change detection analysis, through high-spatial-resolution and high-temporal-resolution imagery to identify windthrow and landslide areas resulting from typhoons.

2.3 Methodology

2.3.1 Study Area

In August 2016, four typhoons hit Hokkaido, the northernmost island of Japan: Chanthu (No. 7, making landfall on 17 August), Mindulle (No. 9, making landfall on 23 August), Lionrock (No. 10, passing very close to the study area on 30 to 31 August), and Kompasu (No. 11, making landfall on 21 August). The wind reached speeds up to 45.5 m/s and was accompanied by heavy rain (Japan Meteorological Agency, 2017) for 15 successive days, producing two major types of damage: windthrow and landslides (Forest Management Division, Bureau of Forestry, Department of Fisheries and Forestry, 2018). In this study, I focused on the detection of the windthrow and landslides immediately after all four typhoons had crossed the island of Hokkaido by 31 August 2016.

This study was conducted at two different study sites in the southeastern part of Hokkaido. According to the local authorities, the outskirts of Setana town suffered from windthrow and landslide damage caused by the typhoons. I defined the first study site, Setana North (42°31'N, 139°58'E), for windthrow detection and the second study site, Setana South (42°22'N, 139°58'E), for landslide detection. Both study sites covered an area of approximately 150 km^2 (Figure 1). Both sites included flat plains and steep mountains varying from 0 m to 1300 m in elevation and were covered by natural forests of *Fagus crenata* Blume, *Betula ermanii* Cham., and *Acer pictum* Thunb. and plantation forests of *Abies sachalinensis* (F. Schmidt) Mast. *and Larix kaempferi* (Lamb.) Carrière.

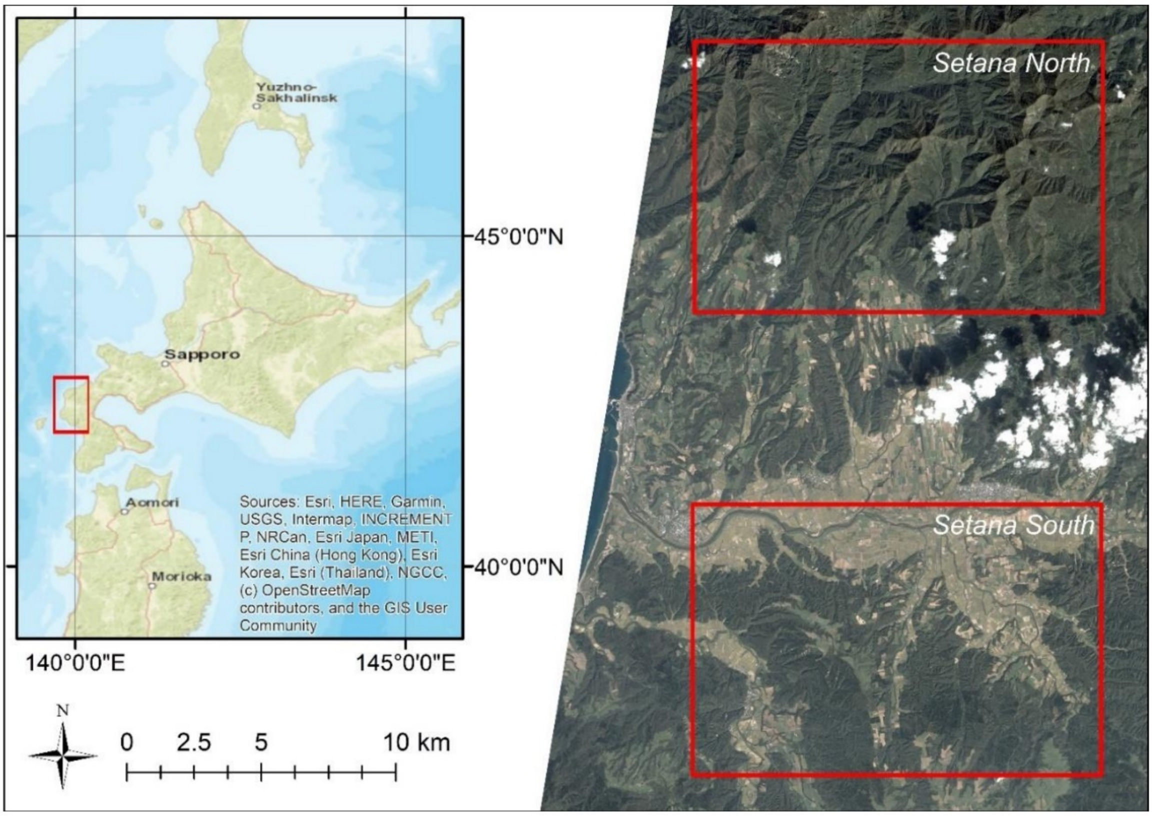

Figure 1. Setana North and Setana South study area with Planetscope data from 21 September 2016.

2.3.2 Datasets

For windthrow and landslide detection, pre- and post-typhoon Planetscope Analytic Product images were acquired (Planet Labs Inc., 2020). Planetscope is a satellite constellation consisting of approximately 120 microsatellites delivering a near-daily temporal resolution. The images have a high spatial resolution of 3 m per pixel, which is suitable according to a field survey performed prior to the study, in four different spectral bands: blue (455–515 nm), green (500–590 nm), red (590–670 nm), and near-infrared (780–860 nm).

The Planetscope Analytic Product offers orthorectified images from which distortions caused by terrain and perspective effects on the ground have been removed, thereby restoring the geometry of a vertical shot, and the data that have been radiometrically calibrated, which produces a surface reflectance product.

For both test sites, I used pre-typhoon images acquired on 27 August 2016, 3 days before the Lionrock typhoon hit, and post-typhoon images acquired on 21 September 2016, 21 days after the typhoons hit. The images from each date were mosaicked, and the urban areas and agricultural fields were masked using forest data provided by the Japanese Ministry of Land Infrastructure Transport and Tourism (Japanese Ministry of Land Infrastructure Transport and Tourism, 2020) that were adjusted to match the Planetscope imagery. For cloud masking, I considered the unusable data mask (udm) file included alongside the Planetscope Analytic Product, which provides information on unusable data such as those affected by clouds. Since the mask did not cover all clouds nor cloud shadows, and the study area being relatively small, I additionally manually masked the clouds and cloud shadows through visual interpretation of the data.

The input for the SAM and SVM classification methods was a composite image created by layer stacking the pre- and post-typhoon mosaics. I layer-stacked the eight bands of the image in the following order: 1. blue (post-typhoon), 2. green (post-typhoon), 3. red (post-typhoon), 4. near-infrared (post-typhoon), 5. blue (pre-typhoon), 6. green (pre-typhoon), 7. red (pre-typhoon), and 8. near-infrared (pre-typhoon). This step was essential for identifying only the changes that occurred between the two dates by constituting a land cover change spectral signature. For the NDVI filtering method, the input data were the NDVI values of the pre- and post-typhoon mosaics.

Additionally, RGB WorldView2 images from 20 August 2017, which were the closest images available from Digital Globe after the typhoons hit, were used to support the digitalization of training samples for the SAM and SVM classification methods. I visually defined the classes of each point for accuracy assessment, as I explain later. This dataset was selected due to its very high spatial resolution of 0.46 m/px, enabling the visual interpretation of the area (Maxar Technologies, 2020).

2.3.3 Windthrow and Landslide Detection

To detect windthrow and landslides in each test site, I used three different classification methods: the NDVI filtering method, SAM method, and SVM method (Figure 2).

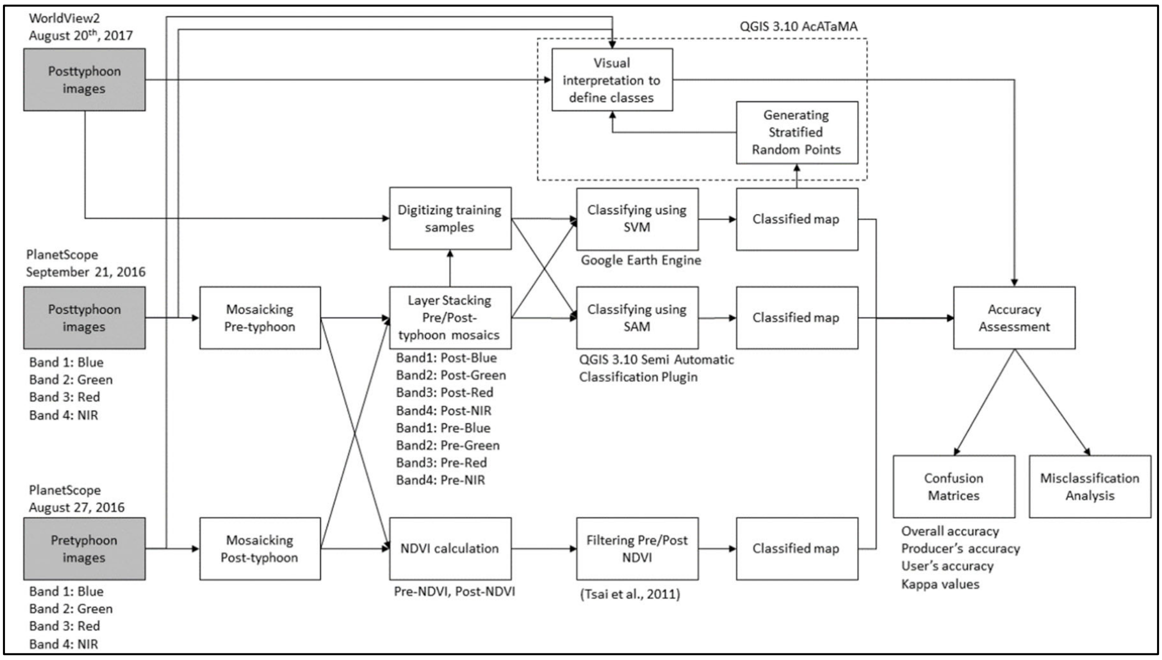

Figure 2. Flowchart of the windthrow and landslide classification and assessment procedure. Input features are identified in the gray boxes.

2.3.3.1 Normalized Difference Vegetation Index Filtering Method

The NDVI is an effective index used to measure the type and amount of vegetation by measuring the difference between near-infrared and red bands, with values ranging between –1 and 1. This index was first presented by Rouse et al. (1973).

The NDVI filtering method for landslide detection shown by Tsai et al. (2011) identifies landslides through the NDVI thresholds T_1 and T_2 using the NDVI filtering rule (Equation (1)).

$$NDVI_{before} - NDVI_{after} >= T_1 \wedge NDVI_{after} <= T_2 \quad \text{(equation 1)}$$

Where:

$NDVI_{before}$= NDVI values obtained from the pre-typhoon mosaic

$NDVI_{after}$ = NDVI values obtained from the post-typhoon mosaic

T_1 and T_2= Threshold value empirically determined

To perform the NDVI filtering method, I used the Map Algebra Function of the Spatial Analyst Package in ArcGIS 10.7, where threshold values were defined based on the NDVI values calculated from the pre- and post-typhoon images. Histograms of known damaged areas were created to support the choice of threshold values along with the visual interpretation of the classified result. The threshold values for Setana North were empirically defined as $T_1 = -1$ and T_2 = 0.65, and those for Setana South were also empirically defined as T_1 = 0.1 and T_2 = 0.6 (Figure 3).

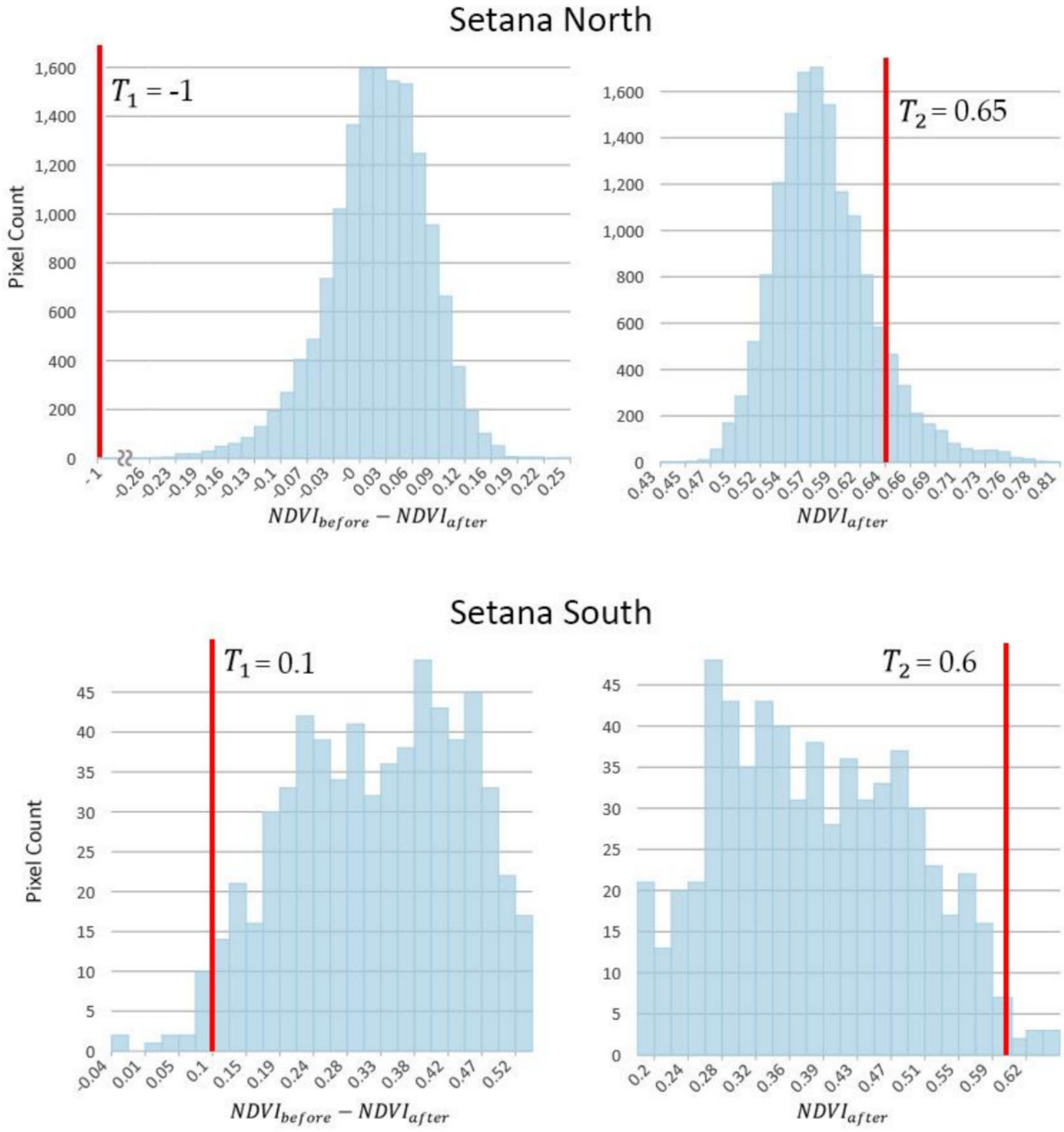

Figure 3. Histograms of damaged areas with the respective threshold values indicated in red. The histogram in the upper left shows Setana North $NDVI_{before} - NDVI_{after}$, and that in the top right shows Setana North $NDVI_{after}$. Setana South $NDVI_{before} - NDVI_{after}$ is displayed in the lower-left corner, and Setana South $NDVI_{after}$ is displayed in the lower right corner.

2.3.3.2 Spectral Angle Mapper Method

The SAM method is a spectral classification method that considers an n-dimensional angle to match the pixel to a reference spectral signature. It calculates the angle between the spectral signature of an image and the spectral signature of a training sample by treating them as vectors.

This technique is insensitive to illumination and albedo effects when used on radiometrically calibrated data. The angle θ was defined by Kruse et al. (1993), (Equation (2)):

$$\theta(x, y) = \cos^{-1}\left(\frac{\sum_{i=1}^{n} x_i y_i}{\left(\sum_{i=1}^{n} x_i^2\right)^{\frac{1}{2}} * \left(\sum_{i=1}^{n} y_i^2\right)^{\frac{1}{2}}}\right) \text{(Equation 2)}$$

Where:

x = spectral signature vector of each pixel from the image

y = spectral signature vector of the training sample

n = number of bands

The pixel matches the class which has the lowest angle (Equation (3)):

$$x \in C_k \Leftrightarrow \theta(x, y_k) < \theta(x, y_j) \forall k \neq j \; and \; \theta(x, y_k) < T \text{ (Equation 3)}$$

Where:

C_k= class k

y_k= Spectral signature of class k

y_j= Spectral signature of class j

T = Threshold to exclude pixels greater than this value

The SAM method was performed using the Semi-Automatic Classification Plugin (Congedo, 2016) in QGIS 3.10 (QGIS Development Team, 2020). Based on composite layer stacked images used as input, training samples were defined by digitized polygons in known damaged areas and checked using the pre- and post-typhoon Planetscope data accompanied by the Worldview2 imagery, and the threshold *T* was defined.

To determine the optimal numbers of training samples and threshold values for windthrow and landslide detection, I tested different numbers of training samples (1, 2, 4, 8, and 16) and different threshold values (1, 4, 7, 10, 13, and 16) and compared the overall accuracies of all combinations (Figure 4).

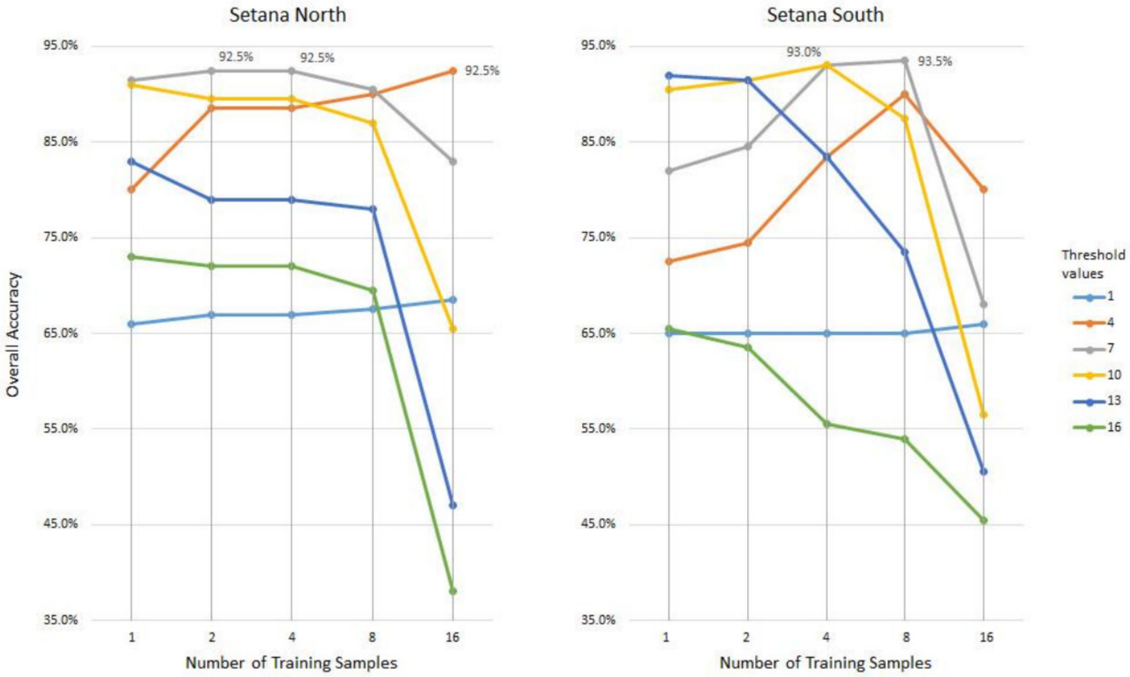

Figure 4. Comparison of combinations of training sample numbers (x-axis) and threshold values according to overall accuracy (y-axis).

The criteria used to define the optimal values for classification were determined by overall accuracy, the number of training samples, and visual interpretation of the final classification result. For windthrow detection in Setana North, the number of selected training samples was 2, with a threshold set at 7 (overall accuracy: 92.5%). Visual interpretation of the classified map revealed some scattered false-positive misclassifications (the classified map defined the area as damaged, but the reference map showed a nondamaged area), so the size and location of the training samples were empirically adjusted to improve the classification.

For landslide detection in Setana South, 8 training samples with the threshold value set at 7 yielded the highest overall accuracy (93.5%); however, visual interpretation of the classification map revealed a large number of scattered false-positive misclassifications. Then, I selected the combination of 4 training samples with a threshold set at 7 (overall accuracy, 93%), which presented a better balance among the number of training samples, overall accuracy, and overall shape of the final map.

2.3.3.3 Support Vector Machine Method

The SVM is a classifier that separates different classes by a hyperplane in an n-dimensional space. Support vectors are data points near the hyperplane that influence the position and orientation of the hyperplane, trying to maximize the margin of the classifier (Cortes & Vapnik, 1995).

The SVM model can handle outliers by creating a soft margin on the classifier; in other words, the SVM allows a certain number of misclassifications to keep the margin as wide as possible so that other points can be classified correctly.

In this study, the SVM method was applied using the Google Earth Engine platform (Gorelick et al., 2017). The stacked and masked composite mosaics were uploaded to the platform, and classification was performed using the SVM classifier with the linear kernel type due to its relatively simple implementation and fast performance (Sharma et al., 2016).

Training samples were created by digitizing polygons in the damaged area, and the cost parameter, which defines the margin of the hyperplane, was set to the default value of 1 to yield the best results in both study areas. I applied the value after confirming that low values such as 10^{-5} reduced the overall accuracy of the final result.

For Setana North, two training samples for windthrow areas (1.0234 ha and 0.4005 ha), two training samples for non-windthrow areas (2.6990 ha and 0.9608 ha), and one training sample for water (5.1028 ha) were selected. The water class was posteriorly merged with the non-windthrow class. In Setana South, I selected two training samples for landslides (0.01843 ha and 0.03507 ha) and two training samples for non-landslide areas (9.9478 ha and 26.4685 ha).

2.3.4 Assessment

Accuracy assessment permits the quantitative analysis of the product of a classifier algorithm through an error matrix, which is a tabular layout that shows the performance of a classifier where each row of the matrix represents the predicted class while the columns represent the actual class (or vice versa). The error matrix can deliver different assessment values, including overall accuracy, user accuracy, producer accuracy, and kappa values (Cohen, 1960; Story & Congalton, 1986).

To generate stratified random points for assessing the accuracy of each classified map with each standard error, I used the AcATaMA plugin (Llano, 2019) for QGIS 3.10 with 100 random points for each class (damage and no damage) from the SVM method classified map, totaling 200 points for each study site. This sampling method was found to be appropriate for simple two-class classification (Donner et al., 2000; Foody, 2004; Rozenstein & Karnieli, 2011).

Then, each random point was visually interpreted, and the land cover class was defined by visually interpreting the pre- and post-typhoon Planetscope images with the very-high-spatial resolution (0.5 m/px) WorldView2 images (Appendix Figure A1) to generate error matrices for each classified map. This process was also performed to define the optimal values for the SAM method.

The error matrices reflected the trend of misclassification in the form of producer accuracy and user accuracy and estimated accuracy in the form of the overall accuracy and kappa values. The misclassification trend among the classification methods was analyzed, especially for the false-positive points of misclassification. The land cover type of each point was visually identified and compared to the spectral signatures based on the points that were correctly classified as windthrow or a landslide.

2.4 Results

2.4.1 Windthrow Detection

For all three classification methods, the damage was concentrated on the western side of the Setana North study site (Figure 5). In a comparison of the damaged area, the SVM method classified 312.8 ha of windthrow, while the NDVI filtering method and SAM method classified 234.0 ha and 203.3 ha, respectively (Table 1).

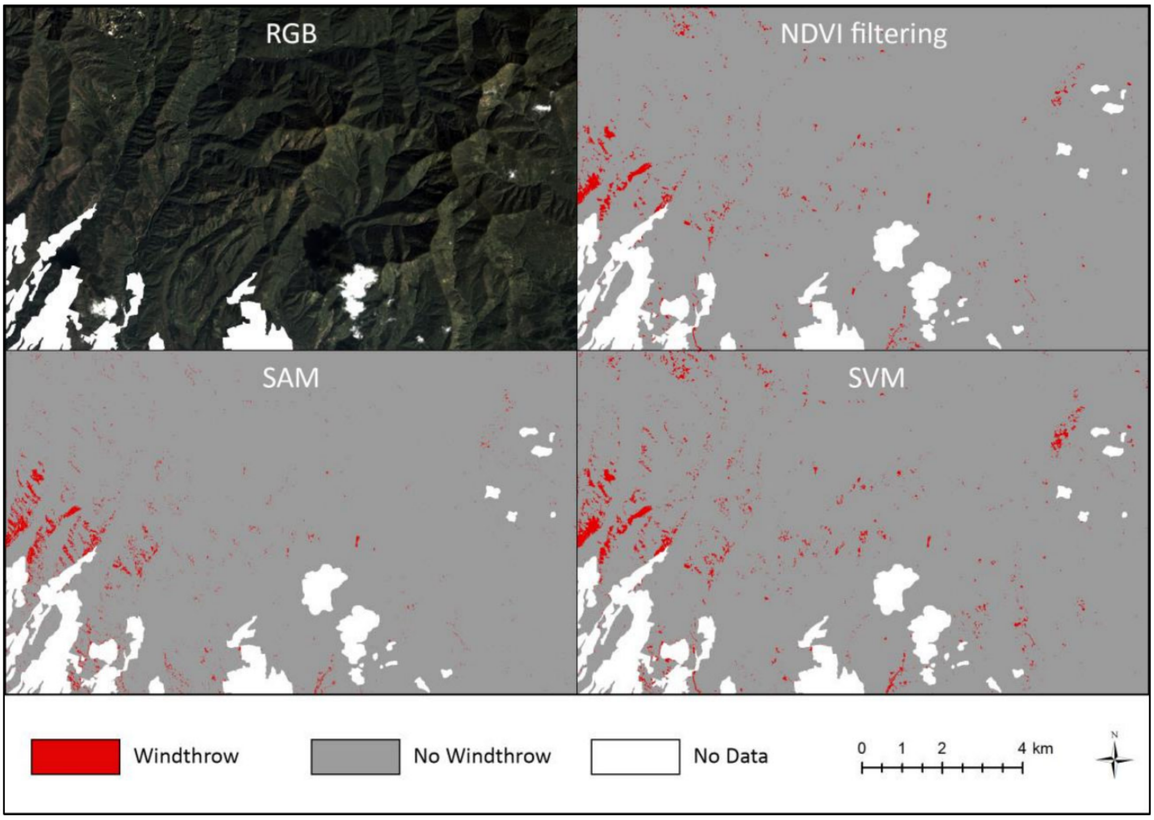

Figure 5. Windthrow classification results in Setana North: Planetscope RGB image, NDVI filtering method results, SAM method results, and SVM method results. The detected windthrow areas are expressed in red.

Table 1. The error matrices of windthrow detection in Setana North.

		Reference					Accuracy	Error
		Damaged	Nondamaged	Total	UA	Area (ha)	OA kappa	Std Error
a) Classified by NDVI Filtering	Damaged	65	29	94	69.1%	234.0	84.0%	0.01593
	Nondamaged	3	103	106	97.2%	13625.1	0.67	
	Total	68	132	200				
	PA	95.6%	78.0%					
b) Classified by SAM	Damaged	56	4	60	93.3%	203.3	92.0%	0.0234
	Nondamaged	12	128	140	91.4%	13655.8	0.82	
	Total	68	132	200				
	PA	82.4%	97.0%					
c) Classified by SVM	Damaged	67	33	100	67.0%	312.8	83.0%	0.00983
	Nondamaged	1	99	100	99.0%	13546.2	0.66	
	Total	68	132	200				
	PA	98.5%	75.0%					

PA: Producer accuracy, UA: User accuracy, OA: Overall accuracy.

Based on the overall accuracy in the error matrices, the SAM method was superior (overall accuracy of 92.0% with a standard error of 0.0234, followed by the other two methods' overall accuracies: 84.0% for the NDVI filtering method with a standard error of 0.0159 and 83.0% for the SVM method with a standard error of 0.0098). The kappa values of the SVM and NDVI filtering methods were over 0.65, which was considered a "substantial level of agreement", while the SAM method had a value of 0.82, which was considered an "almost perfect level of agreement" (Landis & Koch, 1977). Despite the highest overall accuracy, the SAM method presented the lowest producer accuracy value for damaged areas (82.4%: 56/68), while the NDVI filtering method and the SVM method presented higher numbers (95.6%: 65/68 and 98.5%: 67/68, respectively). The lowest producer accuracy for the SAM method reflected the largest number of false-negative points (the classified map defined the area as not damaged, but the reference map showed that the area was damaged). On the other hand, the SAM method yielded the highest user accuracy in damaged areas (93.3%: 56/60), elevating its overall accuracy.

In terms of false positives, the SAM method misclassified only 4 points (forest areas), while the NDVI filtering method and the SVM method misclassified 29 and 33 points, respectively, especially in grassland areas (Table 2). The misclassification from both methods occurred basically at the same points. The spectral signatures between all misclassified points and the windthrow area (Figure 6) presented similar shapes. The variation in each band of the misclassified points was wider than the variation in the windthrow area, mainly in the near-infrared bands (B4 and B8).

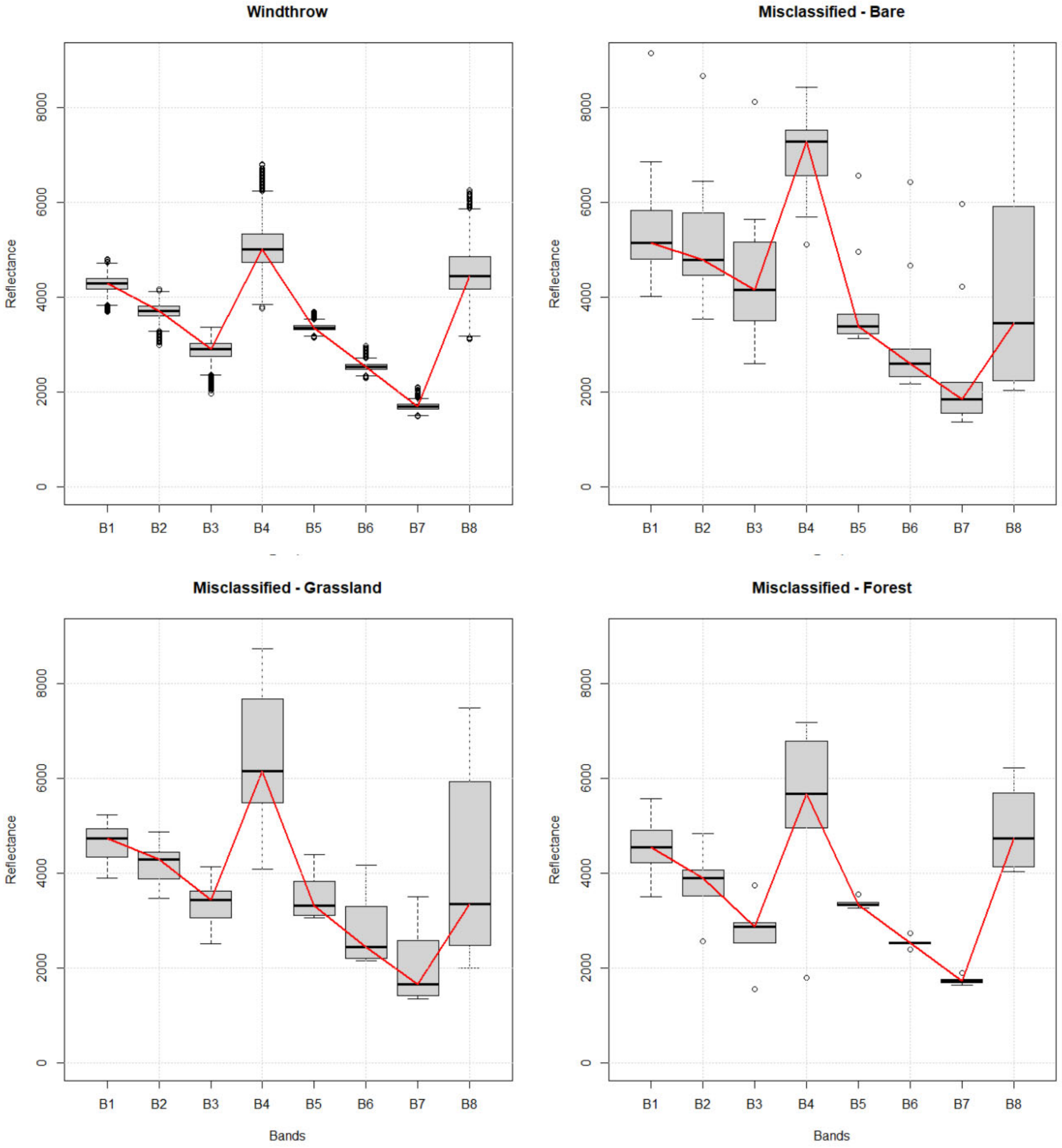

Figure 6. Spectral signature for windthrow taken from the entire windthrow area (upper left: N = 5723) and all different misclassified points of bare land (upper right: N = 14), grassland (lower left: N = 15), and forest (lower right: N = 6). The red line shows the spectral signature from the median values of the data distribution of each landcover type.

Table 2. False-positive misclassified points of windthrow detection in Setana North.

	Bare	Forest	Grassland	Total
NDVI Filtering Method	13	4	12	29
SAM Method	0	4	0	4
SVM Method	13	5	15	33

2.4.2 Landslide Detection

The largest number of landslides was identified in the west-central portion of the Setana South study site (Figure 7). The NDVI filtering method identified 22.0 ha of landslides, while the SAM method and SVM method identified 17.6 ha and 4.7 ha, respectively (Table 3).

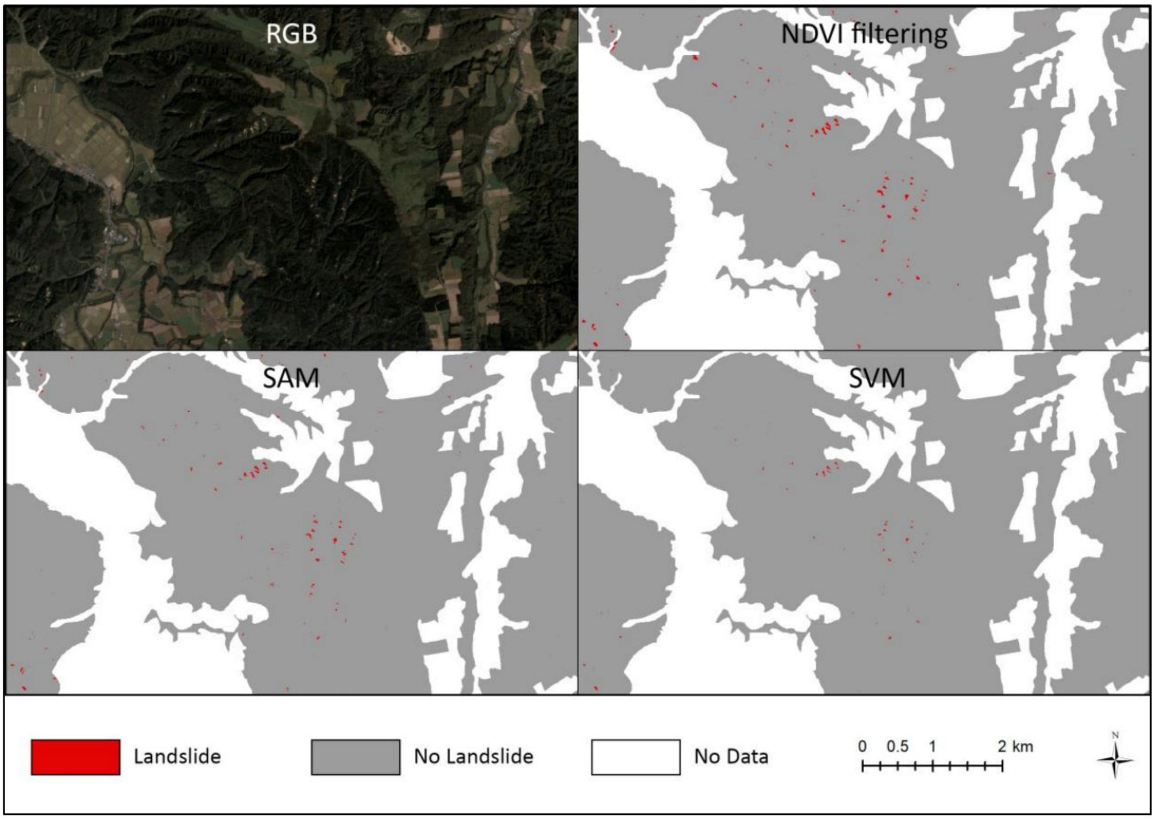

Figure 7. Landslide classification results in Setana South zoomed into the west-central area: (a) Planetscope RGB image, (b) NDVI filtering method results, (c) SAM method results, and (d) SVM method results. The landslide-damaged areas are shown in red.

Table 3. The error matrices of landslide detection in Setana South.

		Reference					Accuracy	Error
		Damaged	Nondamaged	Total	UA	Area (ha)	OA kappa	Std Error
a) Classified by NDVI Filtering	Damaged	69	7	76	90.8%	22.0	96.0%	0.00804
	Nondamaged	1	123	124	99.2%	8039.0	0.91	
	Total	70	130	200				
	PA	98.6%	94.6%					
b) Classified by SAM	Damaged	63	7	70	90.0%	17.6	93.0%	0.01985
	Nondamaged	7	123	130	94.6%	8043.2	0.85	
	Total	70	130	186				
	PA	90.0%	94.6%					
c) Classified by SVM	Damaged	69	31	100	69.0%	4.7	84.0%	0.00999
	Nondamaged	1	99	100	99.0%	8056.1	0.66	
	Total	70	130	200				
	PA	98.6%	75.0%					

PA: Producer accuracy, UA: User accuracy, OA: Overall accuracy.

The NDVI filtering method was significantly superior, with an overall accuracy of 96.0% and a standard error of 0.008. The producer accuracy and the user accuracy of the damaged areas also had values over 90% (Table 3).

The SAM method had the second-best results (93.0% overall accuracy with a standard error of 0.0198), while the SVM method had the lowest overall accuracy of 84.0% with a standard error of 0.0099. The SAM method presented a lower producer accuracy percentage in damaged areas (90.0%: 63/70), while the SVM and NDVI filtering methods had a value of 98.6% (69/70).

The NDVI filtering method had the best results in all aspects, with an overall accuracy of 96.0%, a producer accuracy of 98.6%, and a user accuracy of 90.8%.

The lowest producer accuracy for the SAM method reflected the largest number of false-negative points. In contrast, compared to the SVM method, the SAM method had a higher user accuracy (90.0%: 63/70), and the SVM method had the lowest accuracy (69.0%: 69/100). The kappa values of the NDVI filtering method (0.91) and the SAM method (0.85) reflected an “almost perfect level of agreement”, followed by that of the SVM method (0.66), which represented a “substantial level of agreement”.

In terms of false-positive points, visual interpretation of the random assessment points with WorldView2 imagery revealed that misclassification occurred in bare areas (Table 4); the total number of points misclassified by the SVM method was 31, while the total number of points misclassified by the NDVI filtering method and the SAM method was only 7 (and they were the same points). The bare areas mainly included old landslide areas that occurred before the typhoon event.

Table 4. False-positive misclassified points of landslide detection in Setana South.

	Bare	Total
NDVI Filtering Method	7	7
SAM Method	7	7
SVM Method	31	31

The reflectance of the correctly classified points was slightly higher than that of the misclassified points, and the variation in the spectral signature of the post-typhoon points was larger than that of the misclassified points (Figure 8). Band B4 (near-infrared) presented higher values for landslides than for misclassified points, generating a slight difference in the spectral signatures between them.

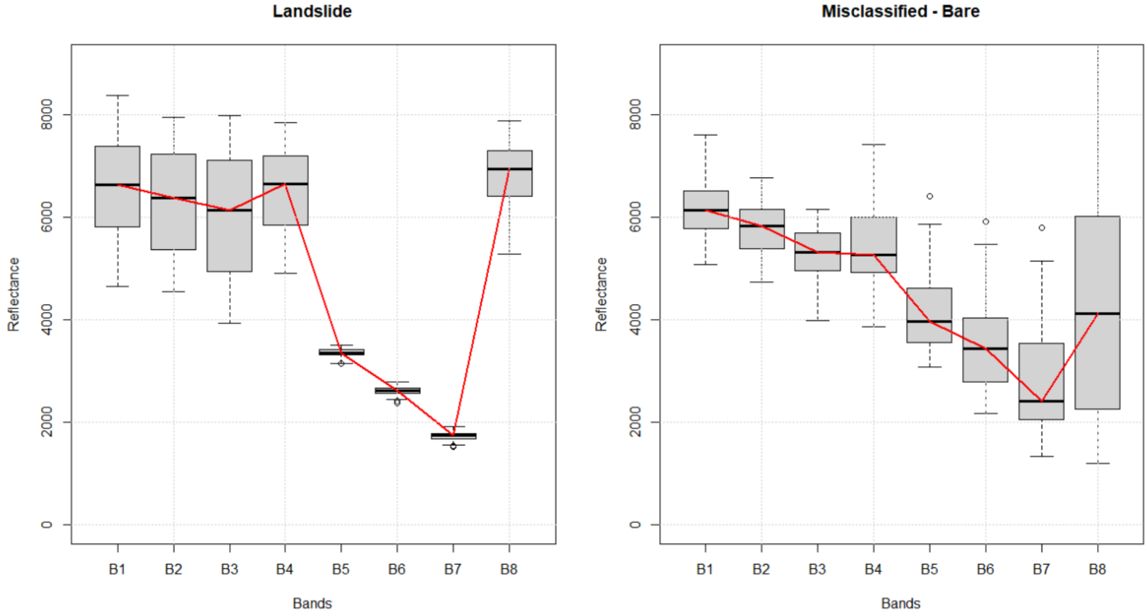

Figure 8. Spectral signature for the entire landslide area (left: N = 156) and all different misclassified bare points (right: N = 31). The red line shows the spectral signature from the median values of the data distribution of each landcover type.

2.5 Discussions

The damaged area by windthrow and landslides after the typhoon hits was detected through Planetscope data. The post-typhoon images were collected 21 days after the last typhoon hit, and no cloud-free images were available during these 21 days. The high temporal resolution of the Planetscope data increased the chances of obtaining cloud-free images. Although these data have a relatively low spectral resolution of only four bands, the results showed that they were suitable for detecting windthrow and landslides using the methodologies adapted in this study.

2.5.1 Performance of Methodologies to identify Windthrow

For windthrow detection, the SVM method classified 312.0 ha of windthrow, 78.0 ha more than the NDVI filtering method, and 109.0 ha more than the SAM method. According to the visual interpretation of each classified map, the SVM method and the NDVI filtering method classified windthrow in less detail than the SAM method. The SAM method could differentiate some parts of the road crossing the windthrow area, while the NDVI filtering method and the SVM method classified the whole area as windthrow, increasing the total area classified as being damaged (Figure 9). All three methods identified the main area of damage on the western side of the Setana North study site. The differences in damage size occurred in areas on the northern and eastern sides of the study site and were also scattered in small areas throughout the study site, and they were generated by misclassification (Figure 5).

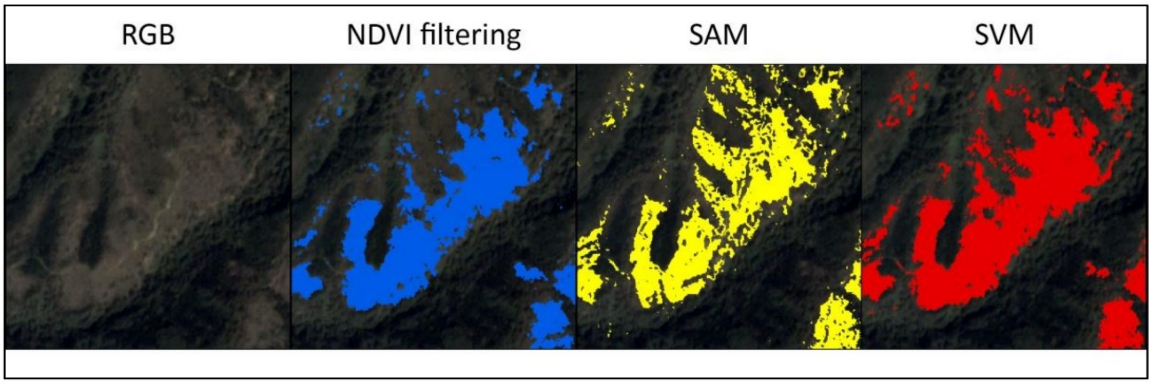

Figure 9. Comparison of windthrow delineations by three methods in Setana North. The SAM method could distinguish some parts of the road crossing the area (the light-colored line in the RGB image) from windthrow.

Misclassification occurred in all three methods but occurred in a larger proportion with the NDVI filtering method and the SVM method. Even though the placement of the misclassified points was almost the same for the NDVI filtering method and the SVM method, the causes for misclassification by the two methods were different. Windthrow areas usually consist of tree foliage, trunks, roots, and soil; the energy reflected from those areas has a similar spectral signature to the forest, grassland, and bare area classes (Figure 6). The broad reflectance variation in each band from the misclassified points increased the complexity of windthrow detection for the SVM method, using the linear kernel type, limiting the performance of the algorithm even with different cost values. SVMs are not optimized for noisy data, which are commonly found in remotely sensed datasets (Mountrakis et al., 2011). On the other hand, the NDVI filtering method is based only on NDVI values; as vegetation remained on the site, the values obtained by the NDVI filtering method could be similar to the values of grasslands and bare areas with some amount of vegetation. The difference between the pre- and post-typhoon NDVI values (Equation (1)) did not contribute to the detection of windthrow, and the final classification was based only on the value of the threshold T_2. For the detection of windthrow in Setana

North, the SAM method had the highest overall accuracy (92%) and kappa value (0.82) when using two training samples and a threshold value of 7 due to its ability to compare spectral similarity between the image and the reference training sample (Petropoulos et al., 2013). The threshold value also helped improve the classification results by not classifying pixels if the spectral angle distance was greater than the T value (Congedo, 2016) and eliminating classification noise throughout the area by limiting the angle distance.

2.5.2 Performance of Methodologies to identify Landslide

For landslide detection in Setana South, the visual interpretation showed that the NDVI filtering method classified the whole landslide area, while the other two methods did not (Figure 10). In contrast to windthrow, landslides usually remove all vegetation, facilitating detection based on NDVI values. Even though the majority of vegetation was removed, the spectral signature of landslides of the reference training samples showed small amounts of remnant vegetation in those areas. Therefore, the SAM method could not correctly classify the areas where the spectral signature showed no vegetation, in turn classifying areas of actual landslides as non-landslide areas. Although the SVM method could classify the areas with a no-vegetation spectral signature, it struggled to identify the borders of landslides, leading to a higher probability of classifying areas with a higher level of vegetation as non-landslide areas.

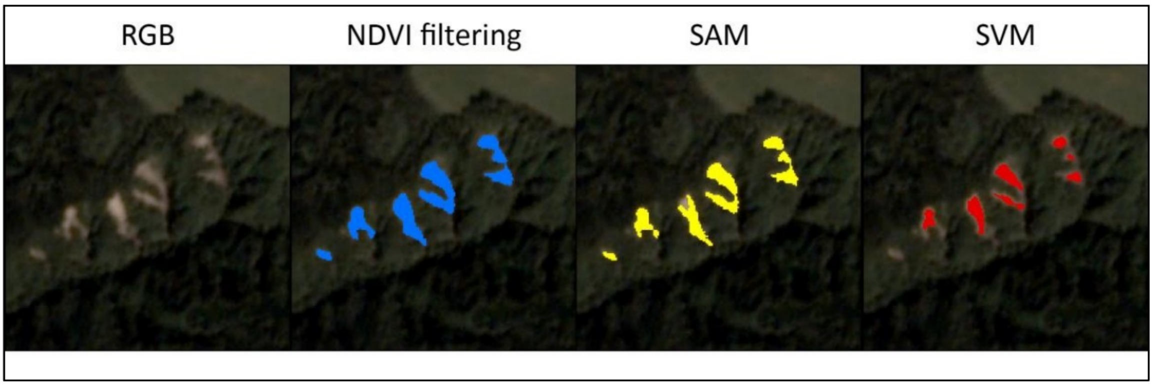

Figure 10. Comparison of landslide delineations by three methods in Setana South. While the NDVI filtering method (blue) classified all areas as landslides, the SAM method (yellow) could not detect some areas (top area of the center landslide), and the SVM method (red) did not classify the borders of the landslide area.

The SVM method identified the smallest landslide area and resulted in the largest number of misclassifications, 31 points, which may have been caused by the same problems presented for windthrow detection due to the similarity of spectral signatures between landslide and bare areas and overfitting. As in windthrow detection, I used the default settings for the SVM method of the Google Earth Engine with the linear kernel, using visually interpreted training samples. I tried to increase the number of training samples, but this did not improve the final result, and cross-validation is recommended to improve the final classification (Hsu et al., 2008).

The SAM method misclassified 7 points, the same points misclassified by the NDVI filtering method. As mentioned before, although the SAM method classified the smallest landslide area due to the difference in spectral signatures, the algorithm had an adequate performance for landslide detection. Compared with the SVM method, this method yielded a higher user accuracy, which represents the probability that the landslide pixel is actually represented on the ground. On the other hand, the SVM method performed better for the no-damage class, elevating its overall accuracy.

The landslide areas were visually washed out completely and did not contain remnant vegetation, but the spectral signature showed that vegetation was present. Although bare areas have a different spectral signature, the reflectance variation in the bands of the post-typhoon landslide spectral signature contributed to the misclassification. One simple way to improve the final classification would be to mask the bare areas that were present before the typhoon event.

The NDVI filtering method yielded the best overall accuracy and kappa values for landslide detection, which is expected due to the characteristics of the NDVI for the evaluation of vegetation amount. The histograms of the landslide areas conveyed clear information to define the threshold values (Figure 3). This result confirms Danneels et al. (2007) statement about landslide classification based on the NDVI producing the best results.

The results obtained from both study sites, combined with the high spatial resolution and horizontal accuracy of the Planetscope data (Dobrinic, 2018), showed that all methods were suitable for windthrow and landslide detection.

The Planetscope dataset played an important role in this research, and a resolution of 3 meters provided enough information to identify the damage without being too detailed (where more processing time and tuning of parameters would be necessary) or too rough (where the spatial resolution mixes different landcover classes together). It is recommended to conduct further studies on datasets with different resolutions.

Overall, the SAM method and the NDVI filtering method were the most reliable for measuring windthrow and landslides, respectively.

In contrast, the SVM method results, processed in Google Earth Engine, performed below our expectations despite being generated by the most sophisticated algorithm. Even though the SVM classifier working with the linear kernel yielded a “substantial level of agreement”, the usage of a different kernel could improve accuracy but would increase the processing time.

2.6 Conclusions

The evolution of remote sensing is introducing new techniques for acquiring more quick and accurate data, and this innovation has resulted in easier workflows that different end-users can take advantage. Although several techniques are available, examinations of the appropriate method for each damage type are missing. In this study, three different conventional remote sensing classification methodologies were compared using high-resolution imagery to identify windthrow and landslides with a simple workflow.

The high temporal and spatial resolution of the imagery played an important role in land cover change detection, in addition to the methodologies applied to identify windthrow and landslides. This result was confirmed by the fact that all three conventional methods, namely, the NDVI filtering method, the SAM method, and the SVM method, combined with the high-resolution imagery, were suitable for windthrow and landslide detection, as judging from kappa values that showed "substantial level of agreement" and "almost perfect level of agreement". One aspect to consider in further studies is the use of different-resolution datasets.

For windthrow, the SAM method performed best because it was able to identify damage even if the spectral signatures of the classes were similar. The NDVI filtering method, although not fully suitable for windthrow detection, performed best in landslide detection. The capability of the NDVI facilitated the distinction between areas with and without vegetation.

Even though the SVM method had lower performance than the other methods for windthrow and landslide detection, it yielded satisfactory results. The usage of different kernel types could potentially improve the performance of the SVM method.

CHAPTER 3: COMPARISON OF RGB AND MULTISPECTRAL UAV FOR MONITORING VEGETATION COVERAGE CHANGES ON A LANDSLIDE AREA

3.1 Abstract

The development of unmanned aerial vehicle (UAV) technologies offers practical methods to create landcover maps for monitoring and management of areas affected by natural disasters such as landslides. The present study aims at comparing the capability of two different types of UAVs to deliver precise information, in order to characterize vegetation dynamics in landslide areas over a period of months. A Red Green Blue (RGB) UAV and a Multispectral UAV were used to identify three different classes: vegetation, bare soil, and dead matter, from April to July 2021. The results showed high overall accuracy (>95%) for the Multispectral UAV, as compared to the RGB UAV, which had lower overall accuracies. Although having lower overall accuracies, the vegetation class determined by the RGB UAV presented high producer's and user's accuracy over time, comparable to the Multispectral UAV results. Image quality played an important role in this study, where higher accuracy values were found on cloudy days. Both RGB and Multispectral UAVs presented similar patterns of vegetation, bare soil, and dead matter classes, where the increase in vegetation class was consistent with the decrease in bare soil and dead matter classes. The present study concluded that the Multispectral UAV is more suitable for characterizing vegetation, bare soil, and dead matter classes in landslide areas while RGB UAV can deliver reliable information for vegetation monitoring.

Keywords: landslides; UAV; multispectral; RGB; vegetation monitoring

3.2 Introduction

The evolution of remote sensing technology allows a feasible method for gathering detailed information for mapping land-cover changes (Hansen & Loveland, 2012), drought monitoring (West et al., 2019), and analyzing complex attributes (Blaschke, 2010; Langner et al., 2012) over space and time. This technology uses different types of sensors onboard satellites, airborne or UAVs, and provides different methods of vegetation classification at large and small scales. Remote sensing offers a practical approach to designing strategies for the management of forest disasters such as evaluating landslide-prone areas through airborne, UAV, and ground-based remote sensing (Casagli et al., 2017), as well as for evaluating changes in vegetation cover after a wildfire by using satellite-based remote sensing and UAV (Martinez et al., 2021).

To deal with the need to assess forest disasters for quick management decisions, the advancement of satellite-based remote sensing applications was initiated for detecting areas affected by natural disasters such as windthrow and landslide for forest restoration or forest disturbance management purposes (Furukawa et al., 2020), such as assessing vegetation recovery (Lin et al., 2004), detecting and mapping (Chen et al., 2014; Hervás et al., 2003) of landslide areas, and creating historical landslide inventories (Martha et al., 2012). Although playing an important role in disaster management, satellite-based remote sensing has some limitations in terms of spatial and temporal resolution of the data. Local cloudiness, low temporal and spatial resolution, and gaps in the image create a complex task for vegetation classification (Al-Wassai & Kalyankar, 2013; Fuentes-Peailillo et al., 2018; West et al., 2019). Recently, very high spatial resolution satellites are available, delivering data of around 30 cm per pixel (Maxar Technologies, 2021); despite a high spatial resolution, this could be a limitation in understanding changes happening on smaller scales (Woodcock & Strahler, 1987). A one-day temporal resolution satellite dataset is also available (Planet Labs Inc., 2020), but cloud cover can still be a hindrance to acquiring the desired dataset.

Nevertheless, the evolution of UAV technologies has brought RGB sensors and multispectral sensors to UAVs for more detailed information as compared to satellite-based remote sensing, making it possible to acquire centimeter-level imagery at any time. In terms of cost and availability, multispectral UAVs cost much more and have lower availability while UAVs coupled with RGB sensors are more affordable and accessible. However, RGB UAVs are limited for remote sensing analysis, especially in complex and heterogeneous forest-covered areas, due to the sensor having an RGB array filter (Vanamburg et al., 2006). Despite these limitations, Ruwaimana et al. (2018) proved that the application of UAVs for vegetation classification on mangrove ecosystems provided higher accuracy concerning object-based and pixel-based classification compared to satellite imagery. The implementation of UAV systems gained attention not only for their efficiency to map land cover (Bellia & Lanfranco, 2019; Kalantar et al., 2017) and vegetation on a coastal dune (Suo et al., 2019) but also as an effective tool in mapping and characterizing burned areas affected by wildfires (Lazzeri et al., 2021), as well as landslide displacement mapping (Lucieer et al., 2014).

Comparison of the performance between satellite images and aerial photos for vegetation mapping (Ruwaimana et al., 2018), test of the applicability of UAVs for mapping and monitoring geohazard areas (Rossi et al., 2018), and characterizing and monitoring landslides (Rossi et al., 2016) have been well documented. Yet there is still a gap in understanding how RGB and multispectral sensors on UAVs perform in assessing the regrowth of vegetation after a natural disturbance such as a landslide. In order to understand the condition of the affected area to make management decisions, it is important to determine the vegetation recovery in a landslide area on a small scale (Dixon et al., 2021; Hirata et al., 2014), and the natural regeneration process on a regional scale. Besides, the presence of debris including fallen trees and litter provides a potential for vegetation regrowth by sprouting and seedbanks and by the colonization of early successional plant species (Chećko et al., 2015; Narukawa et al., 2003; Xiong & Nilsson, 1999). Moreover, vegetation regrowth is slow or non-existent on hillslopes because of unstable bare soil conditions (Buma & Pawlik, 2021).

Therefore, a landslide area was mapped considering three different classes (i.e., vegetation, bare soil, and dead matter) to assess the changes in coverage pattern focusing on vegetation growth throughout four months using two different types of UAV. This study aimed to compare the performance of an RGB UAV and a multispectral UAV using a pixel-based classification approach, to understand how the spectral resolution and the type of sensor can deliver precise information for vegetation mapping on a landslide area. The findings in this study can provide baseline information to forest managers and ecologists in selecting the applicable system and assist in deciding the further management practice in the affected area, especially in understanding post-landslide regeneration. Thus, this study was designed for the following objectives: (1) to understand the differences between the UAV systems in vegetation mapping in a landslide area by assessing the parameters that affect the datasets; (2) to monitor the monthly changes in vegetation, bare soil, and dead matter areas in landslides for vegetation recovery.

3.3 Methodology

3.3.1 Study Area

In 2018, the northernmost main island of Japan, Hokkaido, was affected by the Hokkaido Eastern Iburi Earthquake with a magnitude of 6.7 (Japan Meteorological Agency, 2018) and several aftershocks. The seism triggered over 4000 ha of landslides around western Atsuma town (Zhang & Wang, 2019).

This study was conducted in an area of surface failure of approximately 8 ha in the Uryu District in Atsuma town (42° 43′ 20.3″ N, 141° 55′ 22.5″ E), (Figure 11). The area was characterized by moderate terrain with a predominant slope of an angle of fewer than 40 degrees, and the elevation ranged from 57m to 121m. The soil consisted of Neogene sedimentary rock, i.e., sandstone, siltstone, mudstone, and a conglomerate that was covered by a thick pyroclastic fall deposit from the Tarumae Volcano (Osanai et al., 2019; Zhang & Wang, 2019). The area was covered mostly by deciduous trees, fallen trees, and bare soil, with grasses and shrubs such as Japanese sweet-coltsfoot (*Petasites japonicus* (Siebold et Zucc.) Maxim.), dwarf bamboo (*Sasa* spp.), and wild berries (*Rubus* spp.), etc.

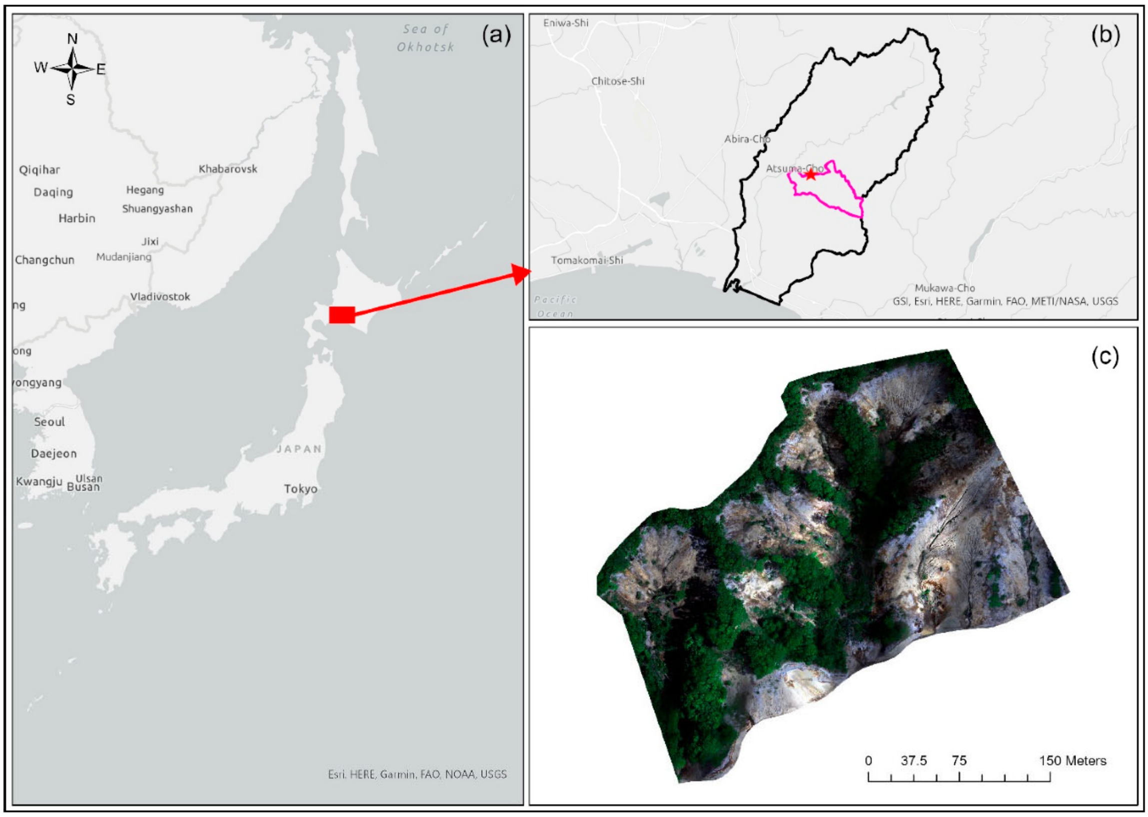

Figure 11. (a) The study area located in Hokkaido, Japan, (b) at Atsuma town (black boundary), and in Uryu district (pink boundary) located at 42°43′20.3″ N, 141°55′22.5″ E (red star); (c) with the true color orthomosaic taken with the Multispectral UAV on 9 June.

3.3.2 Datasets

For the acquisition of the aerial images to create the orthomosaics for analysis, two different UAVs were used: the DJI Phantom 4 Pro and the DJI Phantom 4 Multispectral. The DJI Phantom 4 Pro has a 1-inch CMOS RGB sensor, which acquires the red, green, and blue wavelengths in the same sensor, delivering one 5472 × 3648 pixels RGB image per shot. On the other hand, the DJI Phantom 4 Multispectral has six 1/2.9-inch CMOS sensors, one RGB sensor for visible imaging, and five monochrome sensors for multispectral imaging in different spectral bands: blue, green, red, red-edge, and near-infrared. Each band generates one image of 1600 × 1300 pixels, totalizing six images per shot. The DJI Phantom 4 Multispectral also has a real-time kinematic (RTK)

GNSS system built-in for centimeter position accuracy, but in this study, I compared only the sensors of each UAV: the RGB sensor of DJI Phantom 4 Pro (RGB UAV) and the multispectral sensor from DJI Phantom 4 Multispectral (Multispectral UAV).

The data were taken in four different flight campaigns in 2021: 14 April, 12 May, 9 June, and 9 July, and all images were taken in the morning. The weather condition on 14 April and 9 July was cloudy while being sunny on 12 May and 9 June, with no clouds (Figure 12).

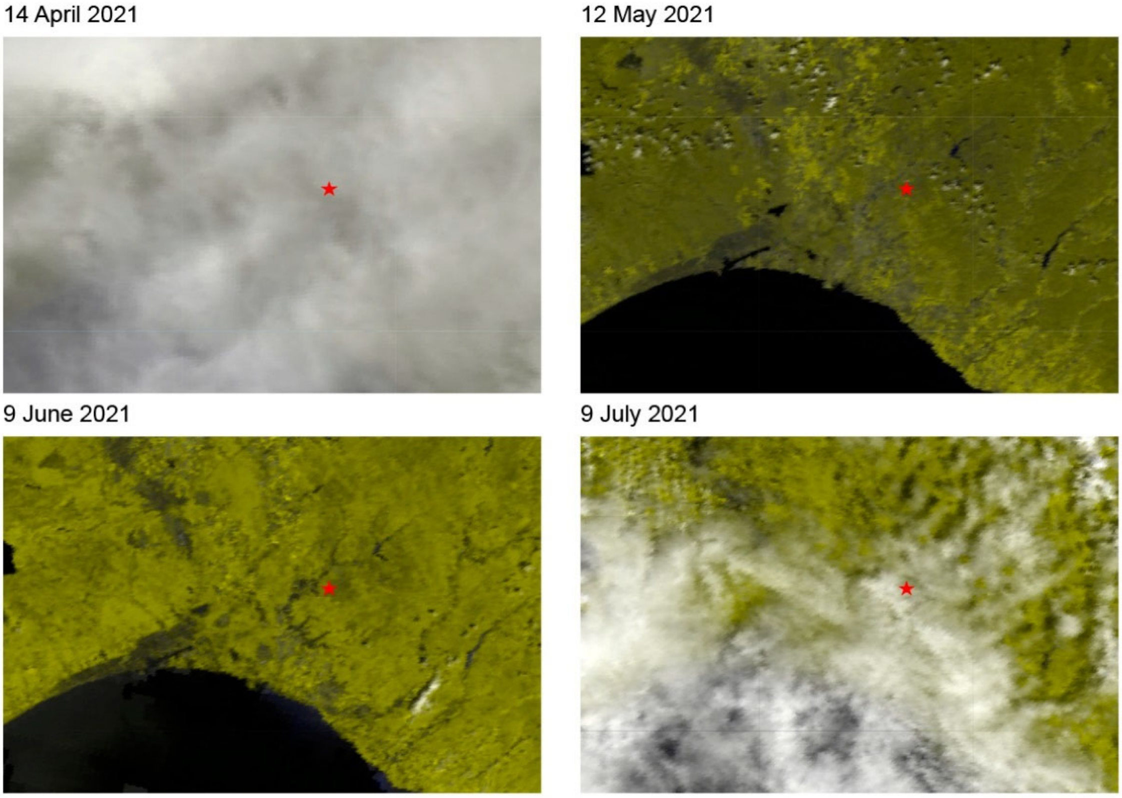
14 April 2021

12 May 2021

9 June 2021

9 July 2021

Figure 12. Cloud cover over the study site (red star) on each date, assessed using Modis M0D09GQ.006 Terra Surface Reflectance Daily Global 250 m, acquired in the morning (*MOD09GQ V006*, 2021).

For each flight campaign, I first flew the Multispectral UAV followed by the RGB UAV (around 14 min each flight), with 5 min in between flights to reduce the displacement of shadow areas. The UAVs flew at 120 m of altitude, capturing images with 80% overlap and 80% side-lap to create the orthomosaics via SfM photogrammetry processing. For the Multispectral UAV, images of a calibration reflectance panel were taken to be used in the calibration of the multispectral images inside the photogrammetry software (*Agisoft Downloads User Manuals*, 2019).

To register the RGB and Multispectral orthomosaics, 15 ground control points (GCPs) made from plywood were placed along with the study site, and the position of each point was collected using the Drogger RTK GNSS system (BizStation Corp, 2021) connected to the ICHIMILL virtual reference station (VRS), (RETSCHER, 2002) service provided by Softbank Japan (*Softbank Ichimill IoT Service*, 2021). The accuracy of each point position was around 2 cm.

For each flight campaign, a field survey was also conducted. Using the Drogger RTK system connected to an android tablet with the open-source application Open Data Kit (ODK), (Hartung et al., 2010), I collected ground truth points to classify the orthomosaics and validated the classification produced from the orthomosaic as explained later. Inside the ODK application, a questionnaire form was previously created containing the classes to be chosen on the field, and photos were taken with the tablet (Figure 13).

Figure 13. (a) The red dot is the vegetation class obtained by ODK with the RTK system accuracy (2 cm) on the Multispectral UAV orthomosaic in true color, and (b) the respective photo of a Japanese sweet-coltsfoot for verification on 12 May.

3.3.3 Data Processing

To create the orthomosaics, I used the SfM photogrammetry technique for UAVs (Remondino et al., 2012), in which each image dataset was processed (*Agisoft Metashape*, 2021) with the GCPs taken on the field to improve the position accuracy of the orthomosaic. For the Multispectral UAV, the 5 monochrome images were automatically merged creating a multispectral orthomosaic, and the images were also calibrated in the software using the calibration reflectance panel images to convert the digital numbers into reflectance values. All orthomosaics were later uploaded into Google Earth Engine (Gorelick et al., 2017) and resampled to the same spatial resolution of 5.5 cm using the bilinear interpolation mode.

3.3.4 Classification and Accuracy Assessment

The processing workflow is shown in Figure 14. To identify vegetation cover in the study area, three different classes were established: vegetation, bare soil, and dead matter (dead leaves, fallen trees, and tree branches). To create the reference dataset, an empirical test was made and 30 samples for each class were selected to conduct the study. The reference dataset was composed of samples taken on the field and samples selected from a visual interpretation of the orthomosaic, totalizing 90 samples. For each date, the same reference dataset was used for the RGB and the multispectral dataset.

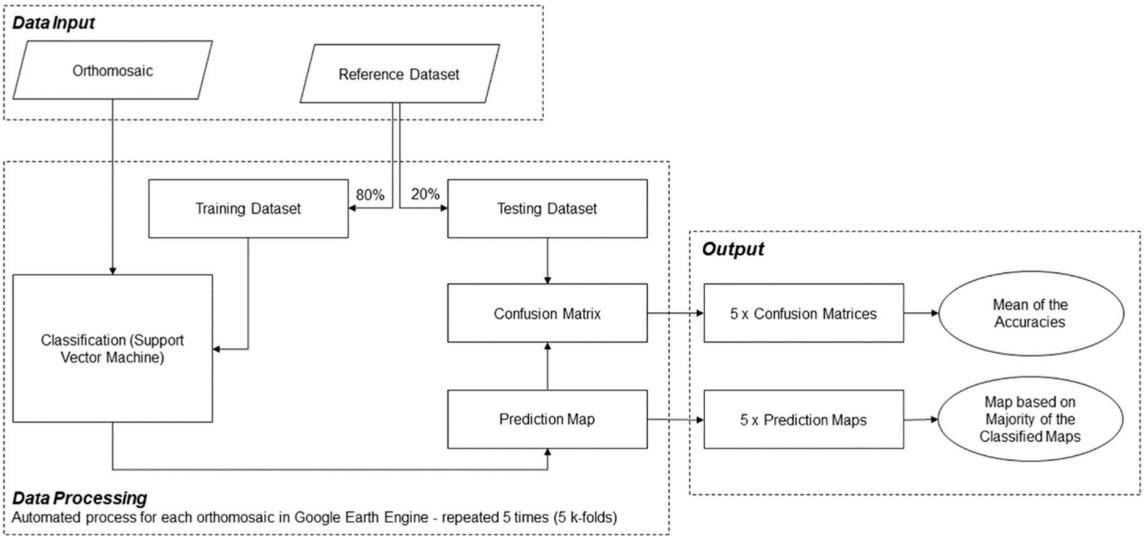

Figure 14. The processing workflow for each dataset.

The classification and the assessment in this study were made by applying the cross-validation method (Mosier, 1951), using 5 k-folds inside Google Earth Engine. The built-in support vector machine classifier with the linear kernel type (Cortes & Vapnik, 1995) was selected to classify the orthomosaics. This method was chosen because of its robustness in assessing the predictor model (Ivanescu et al., 2016), which in this study was mainly influenced by the orthomosaic.

First, the reference data was divided into five different folds randomly, where four folds (80% of the reference dataset) were used to train the classifier and one fold (20% of the reference dataset) to test the classifier. A total of five iterations were made to test all folds.

For each iteration, a classification model was created based on the training dataset and the support vector machine classifier. Then, the classification model generated a prediction map which was put against the independent testing dataset to achieve a confusion matrix. The confusion matrix delivered three different results: overall accuracy, producer's accuracy, and user's accuracy.

The final assessment values for each orthomosaic were created considering the mean of the accuracies of all five confusion matrices. To create the final classification map of each orthomosaic, an aggregation was made considering the majority of classes among the five iterations for each pixel; the final classification map presented a straightforward portrayal of confidence for the study site, which identified the model's fit and stability. Whilst not directly measuring mapping accuracy, the relative confidence of the methodology can provide valuable information to support the interpretation of the maps (Mitchell et al., 2018).

3.4 Results

3.4.1 UAV Orthomosaics

Figure 15 showed that the higher spatial resolution of the RGB UAV created orthomosaics in more detail compared with the Multispectral UAV orthomosaic, even though the data were resampled to 5.5 cm.

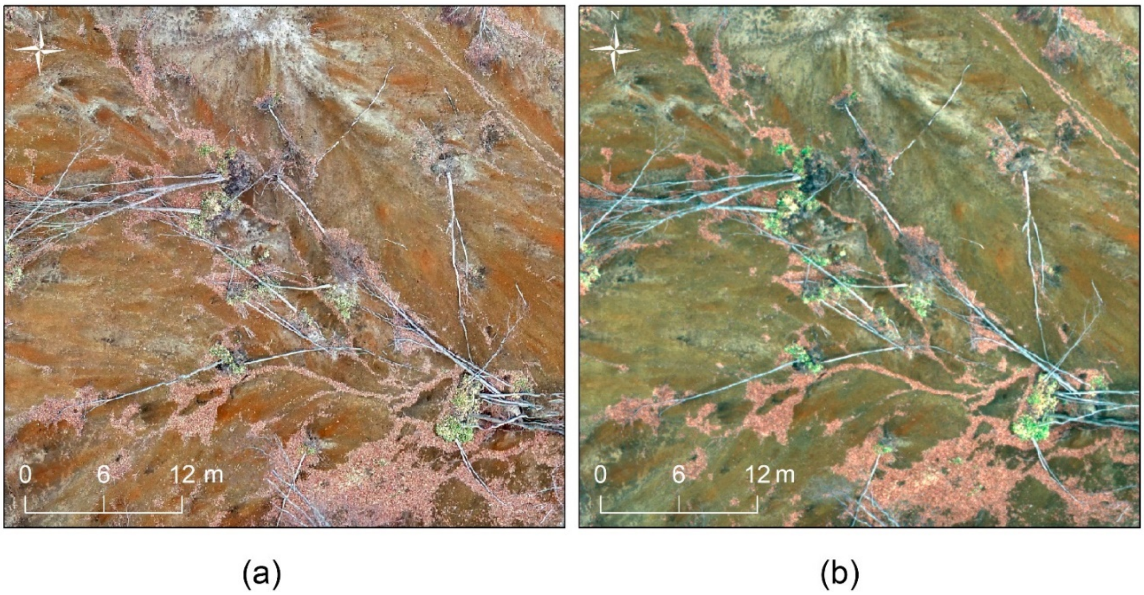

Figure 15. (a) The RGB UAV in true color orthomosaic resampled to 5.5 cm, and (b) the Multispectral UAV in true color orthomosaic resampled to 5.5 cm. The RGB UAV orthomosaic has a sharper image compared to the Multispectral UAV orthomosaic.

The RGB and Multispectral UAV orthomosaic colors and amount of shadow were also influenced by the weather condition (Figure 12). Resulting from the cloudy condition and rain on the previous days of 14 April and 9 July (*Japan Meteorological Agency*, 2021a; *Japan Meteorological Agency*, 2021b), the orthomosaics showed brownish soil without any shadow effect. During the sunny condition on 12 May and 9 June, the orthomosaics showed whitish soil and shadow effects (Figure 16).

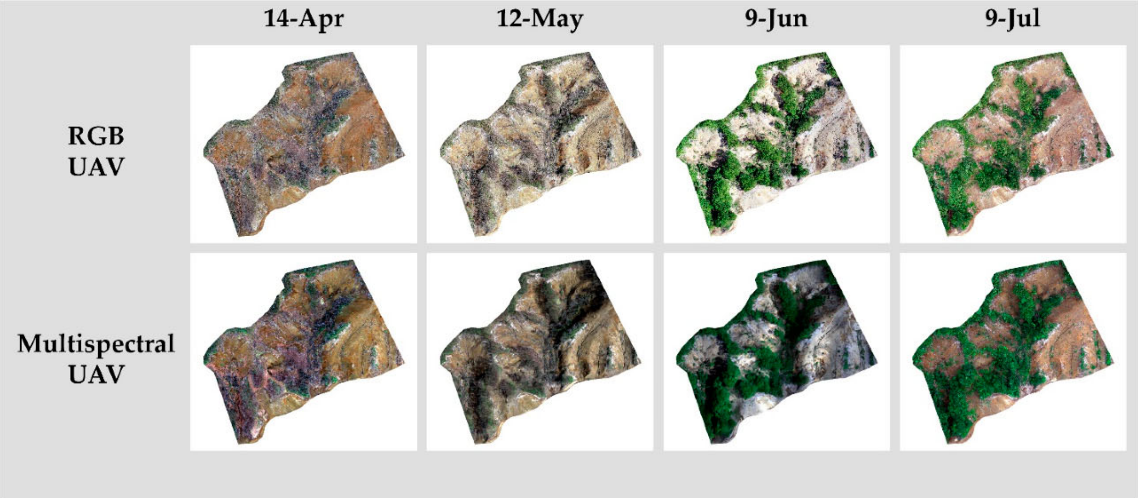

Figure 16. The RGB UAV and Multispectral UAV orthomosaics generated by Agisoft Metashape on 14 April, 12 May, 9 June, and 9 July. The soil color on 14 April and 9 July was brownish with no shadow, while on 12 May and 9 June, the soil was whitish with shadow areas.

3.4.2 Performance of the UAV's Imagery

The performance of the UAV's imagery was accessed considering the overall accuracies calculated from the mean of all five K-folds of each dataset (Table 5). The Multispectral UAV delivered higher percentages of the accuracy (more than 95%) throughout the months. On the other hand, the RGB UAV presented slightly lower overall accuracies, with the highest values on 14 April (94.44%) and on 9 July (90%), while the values were 72.22% and 64.44% respectively for 12 May and 9 June.

Table 5. Overall accuracies for the Multispectral UAV and RGB UAV on each date with the respective weather condition.

		14-Apr	**12-May**	**9-Jun**	**9-Jul**
	Weather	Cloudy	Sunny	Sunny	Cloudy
Overall	RGB	94.44%	72.22%	64.44%	90.00%
Accuracy	Multispectral	97.78%	95.56%	96.67%	98.89%

Looking into the producer and user accuracies of all classes (i.e., vegetation, bare soil, and dead matter), (Table 6), the RGB UAV had the highest values for the three classes on 14 April and 9 July, while lower values were found on 12 May and 9 June, mainly on bare soil and dead matter classes. The Multispectral UAV was more consistent compared with the overall accuracies in Table 5, and both producer and user's accuracies showed high values of >90% throughout the months for all three classes.

Table 6. Producer's and user's accuracy of the vegetation, bare soil, and dead matter classes.

		14-Apr		**12-May**		**9-Jun**		**9-Jul**	
		PA	UA	PA	UA	PA	UA	PA	UA
Vegetation	RGB	100.00%	100.00%	93.78%	88.50%	93.33%	86.00%	100.00%	92.00%
	Multispectral	97.78%	97.14%	96.00%	96.67%	100.00%	100.00%	97.14%	100.00%
Bare Soil	RGB	87.14%	94.17%	43.05%	63.00%	68.00%	46.63%	81.43%	92.67%
	Multispectral	100.00%	100.00%	100.00%	94.64%	96.00%	97.14%	100.00%	100.00%
Dead Matter	RGB	91.00%	94.07%	82.26%	64.12%	49.79%	59.33%	90.64%	84.33%
	Multispectral	96.00%	96.00%	91.31%	97.14%	97.50%	95.00%	100.00%	97.50%

PA: Producer's Accuracy, UA: User's Accuracy.

3.4.3 Classification Results

The classification results created through the aggregation considering the majority classes for the five prediction maps are shown in Figure 17.

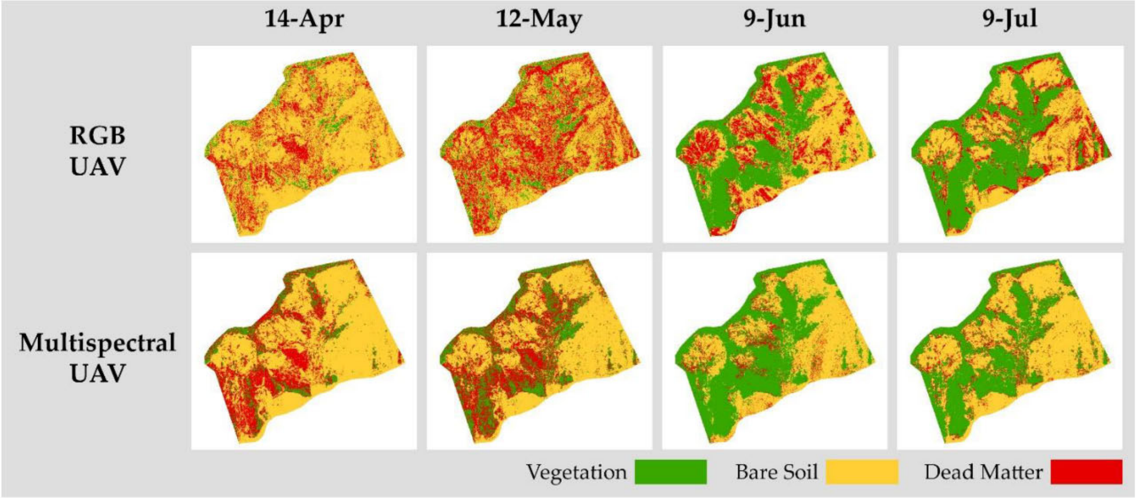

Figure 17. Classification results from the Multispectral UAV and the RGB UAV on each date.

Despite the high accuracy values by the Multispectral UAV, the visual interpretation showed some disparities when compared to the respective orthomosaics (Figure 18). Misclassification mainly occurred in the shadowed area (Figure 18a), where both bare soil and dead matter areas were misclassified as vegetation class (Figure 18b).

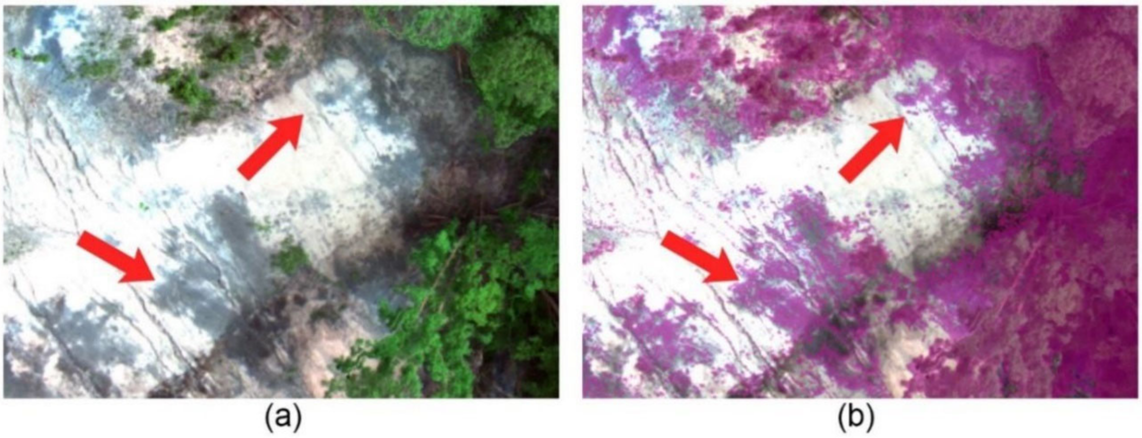

Figure 18. (a) The Multispectral UAV orthomosaic in true color on 9 June, (b) vegetation class (pink), misclassifying bare soil and dead matter areas (red arrows).

The RGB UAV generated more misclassification throughout the study area. On 12 May and 9 June, it was clear to see the misclassification of the dead matter class into bare areas (Figure 16 and Figure 17). A closer look on 12 May (Figure 19) showed misclassification occurring even in no shadow areas.

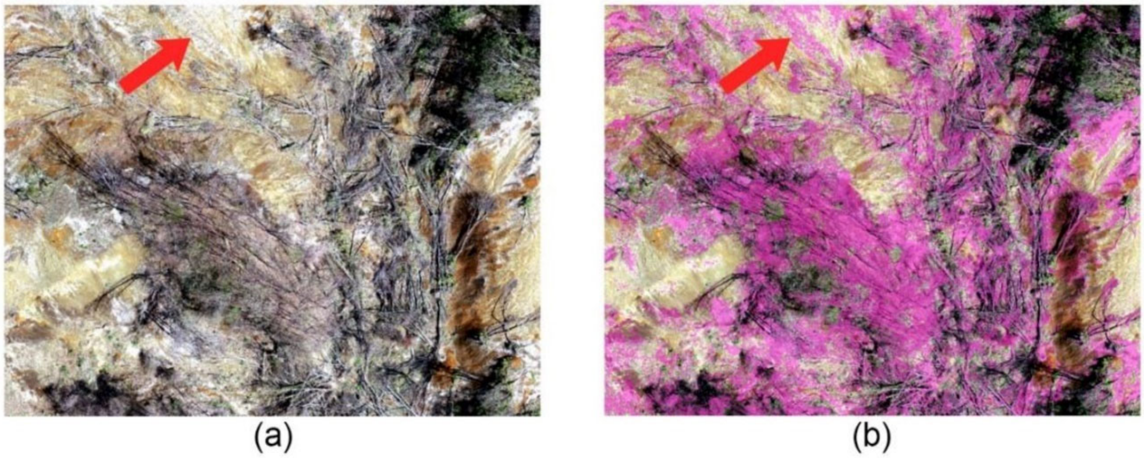

Figure 19. (a) The RGB UAV orthomosaic in true color on 12 May, (b) the dead matter class (pink), misclassifying bare areas (red arrows).

The comparison among the classified maps in terms of class coverage (i.e., vegetation, bare soil, and dead matter) over the months showed a similar pattern in the RGB UAV and the Multispectral UAV from April to June (Figure 20), ratios of the vegetation, bare soil and dead matter classes tended to increase and decrease with time, respectively.

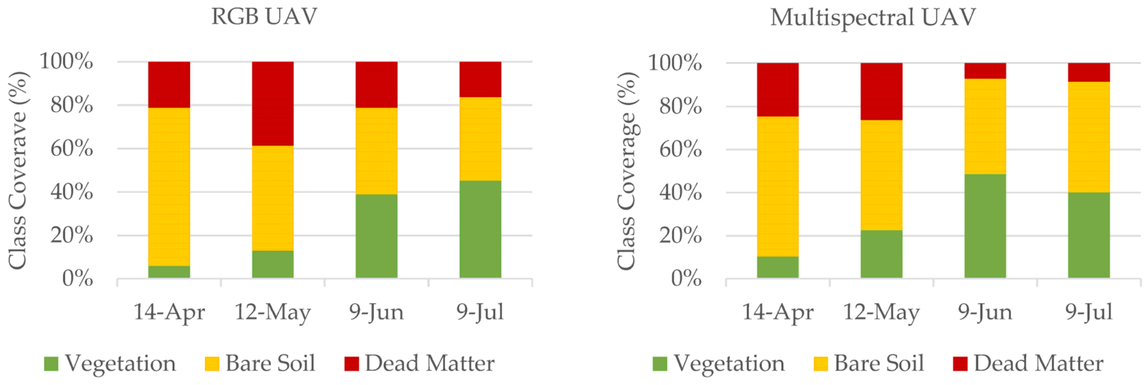

(**a**) (**b**)

Figure 20. The graph shows the class coverage (%) generated from the (a) RGB UAV and (b) Multispectral UAV over time.

In the Multispectral UAV, the proportion for the vegetation class on 9 June was larger than that on 9 July, and the proportion for bare soil class increased during the same period. This resulted from misclassification in the shadowed area on 9 June (Figure 18). Another problem occurred on the RGB UAV, the ratio of the dead matter class increased from 14 April to 12 May. This was caused by the misclassification of the dead matter class into the bare soil class (Figure 19).

Comparing the temporal trend of vegetation class distribution between RGB UAV and Multispectral UAV, a similar spatial pattern of vegetation growth around the already vegetated areas was found (Figure 21). On the other hand, for the bare soil and dead matter classes, the similarities of the spatial pattern were much smaller between the RGB UAV and the Multispectral UAV (Figure 22 and Figure 23), as expected by the low values of the PA and UA accuracies from these classes on the RGB UAV.

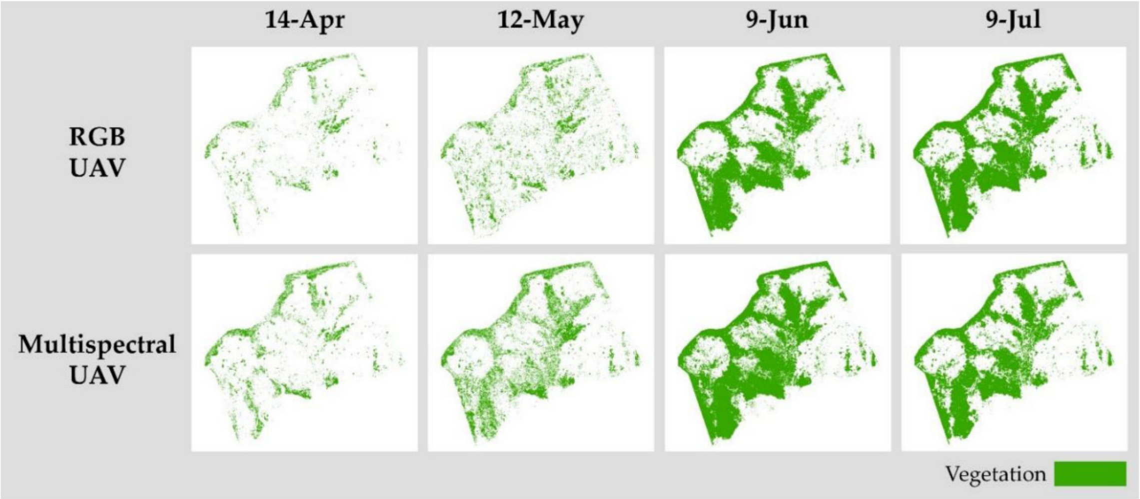

Figure 21. Change of vegetation class over the months from the RGB and multispectral UAV.

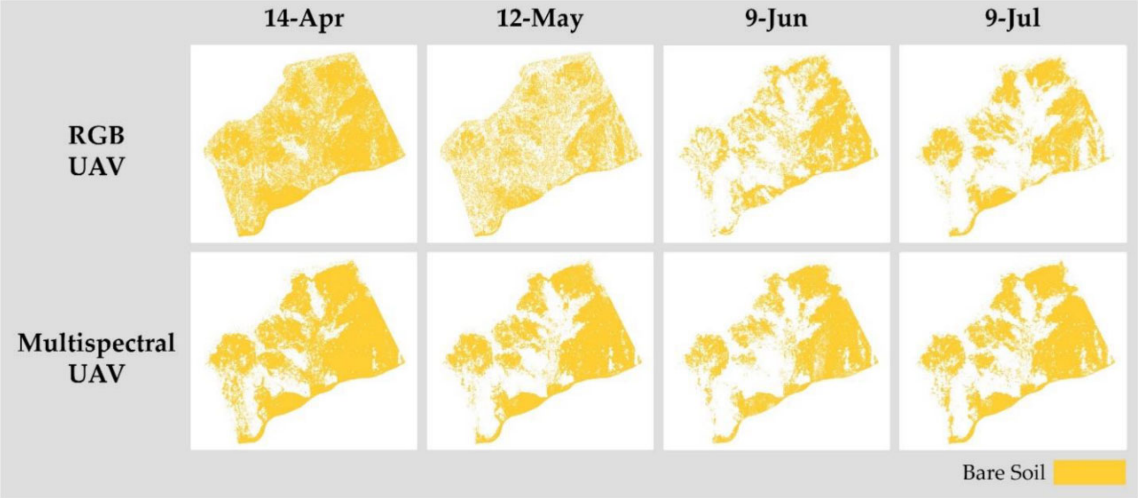

Figure 22. Change of bare soil class over the months from the RGB and multispectral UAV.

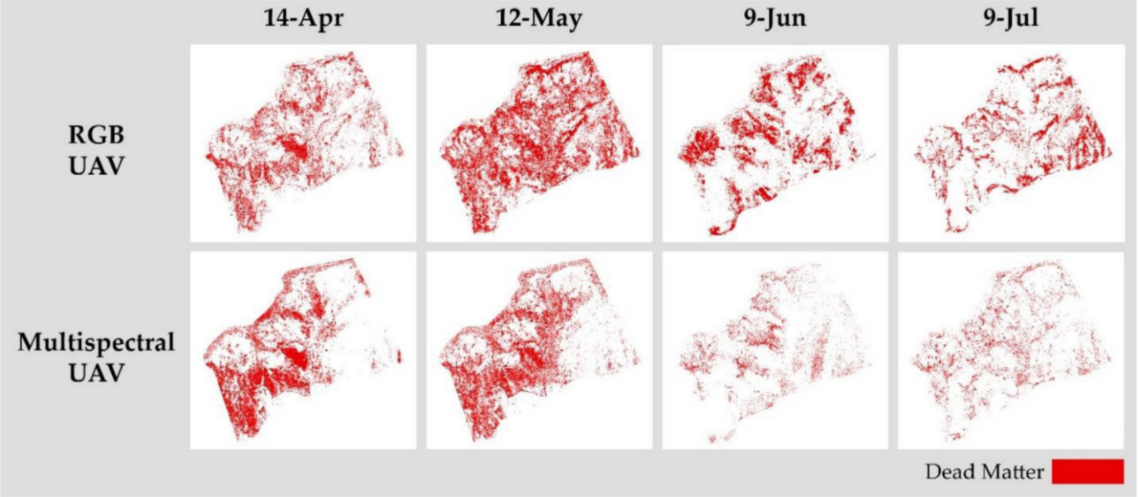

Figure 23. Change of dead matter class over the months from the RGB and multispectral UAV.

3.5 Discussions

3.5.1 Comparison Between the RGB UAV and the Multispectral UAV

The evaluation of the performance of classification into vegetation, bare soil, and dead matter classes of each UAV showed that the Multispectral UAV delivered more consistent results for every class (Table 6), while the RGB UAV, even using higher spatial resolution, because of the smaller number of bands and the type of sensor (Coburn et al., 2018), produced a more speckled classification map. On the other hand, the Multispectral UAV generated some misclassification, mainly in shadowed areas (Adler-Golden et al., 2002; Duffy et al., 2018) irrespective of its five distinct spectral bands and higher accuracy values.

As misclassification was frequent in shadowed areas (Figure 18), the weather conditions played an important role in this study, mainly for the RGB UAV. Cloudy days with brownish soil had better results compared to sunny weather with whitish soil, yielding higher accuracy values for both RGB UAV and Multispectral UAV. The same tendency was shown in Duffy et al. (2018), which suggested that cloudy days had consistent lighting conditions, improving the homogeneity of the spectral signatures.

Although the RGB UAV and the Multispectral UAV generated misclassifications, they could still provide valuable information regarding the monitoring of classes' coverage changes in a landslide area. The RGB UAV indicated an impressive ability to monitor vegetation growth in detail despite the low cost of the system.

The Multispectral UAV is appropriate for pixel-based classification approach because the UAV uses the red edge and near-infrared wavelengths, which are optimal for vegetation analysis. On the other hand, the higher spatial resolution of the RGB UAV could enable a more accurate visual inspection of the geohazard areas as reported by Rossi et al. (2016). Future studies using an object-based classification, which is based on the aggregation of spectrally homogenous pixels through an image segmentation algorithm to then be classified, are suggested to understand the difference between the two UAV systems considering a spatial resolution (Ruwaimana et al., 2018). Therefore, both the RGB UAV and the Multispectral UAV proved to be suitable for the evaluation of the area under a natural regeneration process, at a centimeter-level.

3.5.2 Vegetation, Bare Soil, and Dead Matter Monitoring

The results showed that the UAV was able to analyze both temporal and spatial changes in disturbed areas. Therefore, the UAV is effective in the analysis of the revegetation process of landslide areas. The methodology adopted in this study is probably and especially applicable to temporal changes where the UAV can observe the state of the forest floor when the trees are naked.

The vegetation growth around the vegetated areas confirms that the condition of unstable soil after landslides, prevents seeds from nearby intact forests to germinate due to the erosion of soil, infertile soil, and other abiotic factors, slowing down or preventing the regeneration process. The abundant dead plant materials, i.e., fallen trees and leaf litter, favors the initial stage of plant succession in the landslide area (Shiels et al., 2006; Walker et al., 1996) by protecting the seeds or saplings from soil erosion, as well by improving soil fertility through the decomposition of dead materials.

The expansion in vegetation coverage observed during the four consecutive months suggested that through the increase in vegetation the landslide area may improve ground stability, and the turning of seed germination and the growth of saplings may be accelerated, although the natural regeneration would take a long time (Guariguata, 1990; Walker et al., 1996). Thus, monitoring the temporal changes of spatial patterns such as vegetation, bare soil, and dead matter, contributes to a more detailed ecological research planning. Due to the role of landslide areas in regenerating high vegetation species richness after disturbances (Guariguata, 1990; Pang et al., 2018), the annual vegetation growth dataset is suggested to infer the potential of the study area for natural regeneration.

3.6 Conclusions

The present study revealed that Multispectral UAVs are more applicable to distinguishing vegetation, bare soil, and dead matter areas in landslides. In addition, cloudy weather and brownish soil are recommended to create a more reliable dataset. However, the RGB UAV can play an important role if the purpose is to monitor vegetation development, especially in terms of accessibility and availability of the technology. The monitoring of vegetation, bare soil, and dead matter classes over four months showed the potential initial recovery of vegetation in the landslide area. This indicates that the monthly and multi-year dataset will serve a better understanding of the process of initial vegetation recovery. Future work is suggested using an object-based classification, in order to take advantage of the higher spatial resolution of the RGB UAV dataset.

CHAPTER 4: UAV VIDEO-BASED APPROACH TO IDENTIFY DAMAGED TREES IN A WINDTHROW AREA

4.1 Abstract

Disturbances in forest ecosystems are expected to increase by the end of the twenty-first century. An understanding of these disturbed areas is critical to determining management measures to improve forest resilience. While some studies emphasize the importance of quick salvage logging, others emphasize the importance of the deadwood for biodiversity. Unmanned aerial vehicle (UAV) remote sensing is playing an important role to obtain information in these areas through the structure from motion photogrammetry process. However, the technique faces challenges due to the fundamental principle of structure from motion photogrammetry as a passive optical method. In this study, I investigated a UAV video-based technology called full motion video to identify fallen and snapped trees in a windthrow area. I compared the performance of full motion video and an orthomosaic, created by the structure from motion photogrammetry process, to manually identify fallen and snapped trees, using a ground survey as a reference. The results showed that full motion video was able to identify damaged trees because of the better context awareness provided by the video compared with the orthomosaic, although providing lower position accuracy. In addition to its simple processing, full motion video technology showed great potential to support the interpretation of conventional UAV remote sensing analysis and ground surveys, providing rapid and reliable information about damaged trees in windthrow areas to forest managers.

Keywords: UAV, full motion video; windthrow; fallen trees; snapped trees

4.2 Introduction

In Eastern Asia, typhoons are one of the main natural hazards affecting forest ecosystems (Dale et al., 2001; Mabry et al., 1998). An expansion of disturbed forest ecosystems is expected to increase with the increase of intense tropical cyclones predicted by the end of the twenty-first century (Murakami et al., 2012). Understanding the ecological resilience of forest ecosystems to natural and human impact is critical for identifying the optimum management measures (Morimoto & Negishi, 2019; Thompson et al., 2009; Waldron et al., 2013). While some studies emphasized the importance of quick salvage logging to dampen insect outbreaks in windthrow areas (Dobor et al., 2020; Leverkus et al., 2021), other studies emphasized the ecological importance of the deadwood left from these natural hazards (Cooper-Ellis et al., 1999; Mori et al., 2017; Morimoto et al., 2019; Siitonen, 2001) and the importance of individual deadwood management to benefit the biodiversity of disturbed areas (Jonsson et al., 2005; Vítková et al., 2018).

The development of remote sensing has brought many tools and techniques to manage areas affected by natural disasters (Furukawa et al., 2020; Im et al., 2019), with different sensors onboard satellites, airborne, and UAVs acquiring remotely sensed data to monitor disturbed areas. Recently, UAVs have been playing an important role in remote sensing because of their ability to capture a variety of very high-resolution datasets at any time (Alvarez-Vanhard et al., 2021; Mohd Daud et al., 2022). A widely used UAV remote sensing technique is the SfM photogrammetry (Iglhaut et al., 2019), which enables the creation of two-dimensional (2D) and three-dimensional (3D) datasets to analyze areas affected by natural disasters (Furukawa et al., 2021; Gomez & Purdie, 2016).

However, UAV SfM photogrammetry faces challenges such as long processing time, difficulty to visualize high-resolution point clouds in GIS, reproduction of complex areas such as those found in forests and steep terrains, susceptibility to lighting conditions, and only one perspective from the target (Berra & Peppa, 2020; Furukawa et al., 2021; Inoue et al., 2014; Rothmund et al., 2017). Some of these challenges are often related to the fundamental principles of SfM photogrammetry as a passive optical method (Iglhaut et al., 2019). Lidar is an option to overcome some limitations of UAV SfM photogrammetry techniques, such as the complicated and unreliable matching process, especially when dealing with significant depth variation (Habib et al., 2004), but it is still expensive requiring high skilled personnel and high computational processing (Chirici et al., 2018; Dandois & Ellis, 2010).

Another way to overcome the limitations of SfM photogrammetry techniques is videography. Some studies using video streams combined with GIS were used for forest fire prevention (Fang et al., 2008), and to assess forest damage caused by hurricanes (Jacbos & Eggen-McIntosh, 1993). The development of video and GIS technology brought a technology called full motion video (FMV). The technology consists in combining automatically the video with GIS through a multiplexing process. FMV can also provide telestration capabilities, allowing analyzing and editing of feature data inside the video and automatically generating features inside the GIS (Esri, 2022b).

Considering the importance of management of individual deadwood, in this study, the usage of FMV technology was examined to identify fallen (i.e. uprooted trees and stems on the ground) and snapped trees in a windthrow area. In specific, the feature data created from FMV and orthomosaic (produced by the UAV SfM photogrammetry process) were compared with a ground survey as a reference, and the strengths and weaknesses of the FMV technology to monitor damaged trees in a windthrow area were evaluated.

4.3 Methodology

4.3.1 Study Area

In September 2004, the Typhoon Songda hit northern Japan and destroyed 369.6 km² of forests. Of the total windthrow area, 30% occurred around Chitose City and Tomakomai City in Hokkaido, Japan (Tsushima & Saitoh, 2005). For this study, I selected an area of 0.37 ha in the national forest in Chitose City (42°45’43.9” N, 141°30’03.3” E) at 150 m of altitude (Figure 24).

Figure 24. a) The study area located in Hokkaido, Japan (red circle), b) inside the national forest in Chitose City (red cross); and c) the orthomosaic with the ground control points (in blue).

The topography of the study area was flat with the soil composed of volcanic ash and pumice. The annual temperature and precipitation averages are 7.1°C and 1384 mm respectively with the dominant tree species of the natural forest being *Abies sachalinensis* (F. Schmidt) Mast. and *Quercus crispula* Blume. After the typhoon, no human intervention was conducted; thus during the data collection, the deadwood was found together with the vegetation recovered after the windthrow (Morimoto et al., 2011).

4.3.2 Data Acquisition

The data for this study was collected on December 7, 2021, 17 years after the Typhoon Songda. The aerial data for this study (still images and video) were taken using the DJI Phantom RTK UAV with a 1-inch CMOS RGB sensor delivering images of 5472 x 3648 pixels and 4K (4096x2160 pixels) resolution video (DJI, 2022). The UAV was also coupled with a built-in RTK system connected to the ICHIMILL virtual reference station service provided by Softbank Japan (*Softbank Ichimill IoT Service*, 2021) to improve the position and altitude accuracy of the aircraft (Feng & Wang, 2008).

To create the FMV compliant data, the UAV was flown using the SiteScan LE application for iPad (Esri, 2022c). This application was necessary to convert the geospatial metadata generated from the UAV to MISB standards (Geospatial Intelligence Standards Working Group, 2022) to be combined with the video file in the multiplexing process. The flight was done at 30 m above the ground and followed automatically a predefined route with the gimbal angle set at 20 degrees, and the video set at 4K resolution in 24 frames per second.

Apart from the video, a total of 145 images were taken at 30 m above the ground, with both overlap and sidelap of 80% to create an orthomosaic. To improve the orthomosaic accuracy, 4 ground control points were placed on each corner of the study site (Figure 24c), and the position of each ground control point was determined using the

DG-PRO1RWS RTK system connected to the ICHIMILL virtual reference station service delivering accuracies within centimeter-level (BizStation Corp, 2021).

A ground survey was conducted on the same day. Because the dense juvenile trees (Morimoto et al., 2021) blocked the way, it was not possible to take samples of all fallen and snapped trees from the whole study area. The sample position of fallen and snapped trees were taken in accessible areas using the RTK system, which corresponded to around 78% of the total area (Appendix Figure A2); where for each fallen tree, two GNSS coordinates were taken (one at each end of a fallen tree), and for each snapped tree, one GNSS coordinate was taken. The height and diameter of the snapped trees were also measured from the photos taken in the ground survey with a reference pole.

4.3.3 Data Processing

The data processing workflow was shown in Figure 25. I used three different data sources to identify fallen and snapped trees in the study area: FMV, orthomosaic, and the ground survey.

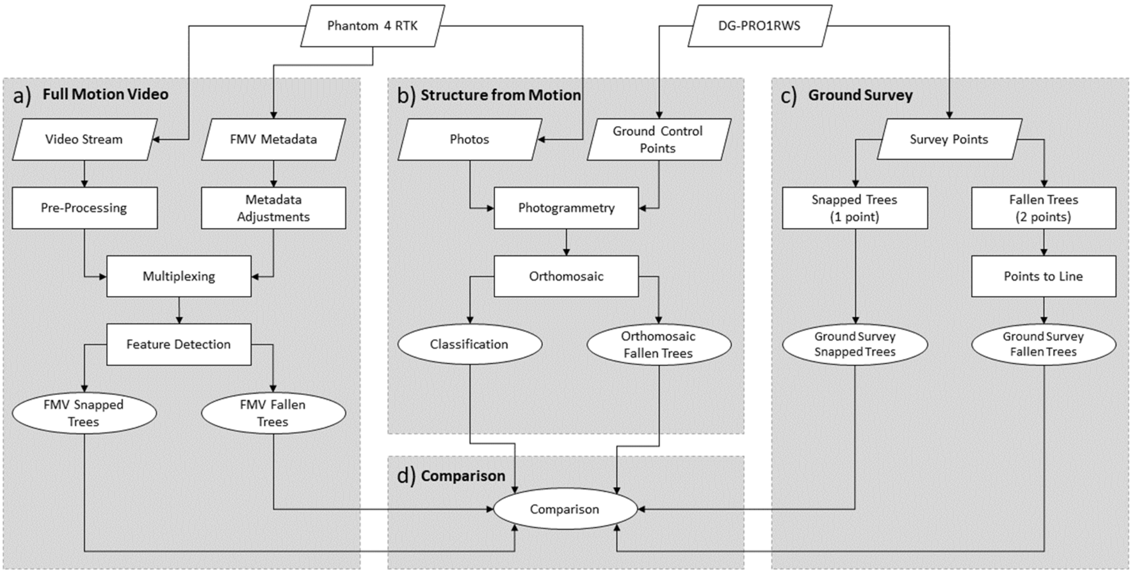

Figure 25. The processing workflow for this study: a) FMV processing, b) SfM processing, c) ground survey processing, and d) comparison of the methods.

4.3.3.1 Full Motion Video Processing

To create the FMV compliant data, the video was combined with the metadata generated from the SiteScan LE application on the iPad using the video multiplexer tool inside the image analyst extension for ArcGIS Pro 2.8 (Esri, 2022a). The video was converted into full HD (1920x1080 pixels) resolution to improve the playback inside ArcGIS Pro, following ESRI’s recommendation. To align the video footprint in GIS, some adjustments had to be done according to the parameters supplied by ESRI’s support team.

After combining the video with the metadata, the whole study area was visually interpreted throughout the video frame by frame. The feature data was created inside the video, automatically generating feature data inside the GIS (Figure 26). One feature line was created for each fallen tree, and one feature point for each snapped tree.

Figure 26. a) The video where I identified the fallen and snapped tree, b) GIS with the orthomosaic and the video footprint (in yellow).

4.3.3.2 SfM Photogrammetry Processing

To create the orthomosaic, the SfM technique (Remondino et al., 2012) was done on Agisoft Metashape (*Agisoft Metashape*, 2021). Combining all 145 images with the 4 ground control points generated an orthomosaic with 0.793 cm per pixel of spatial resolution with a horizontal accuracy of 0.77 cm.

Through visual interpretation of the generated orthomosaic, feature lines were manually created to identify fallen trees in the whole study area. For snapped trees, the identification was not possible since only the top of the snapped tree could be seen from the orthomosaic.

A classification map was also created from the orthomosaic to examine how the environment affected the identification of fallen and snapped trees in the windthrow area. The classification map was divided into 3 classes: vegetation with leaves, vegetation without leaves, and non-vegetation. The vegetation with leaves class consisted mostly of coniferous trees, while the vegetation without leaves class consisted of deciduous trees and deciduous shrubs. The non-vegetation class consisted of areas that were exposing everything, such as soil and deadwood on the ground surface.

4.3.3.3 Ground Survey Processing

After collecting the GNSS coordinates from the fallen and snapped trees with the RTK system on the field, the data was imported into ArcGIS Pro and converted the coordinates into feature data. For fallen trees, the coordinates located at each end of a fallen tree were connected creating a feature line. For snapped trees, the coordinates were only converted into feature points. The feature's position accuracy was at centimeter-level (BizStation Corp, 2021).

4.3.4 Comparison

To compare the feature data resulting from the 3 types of processing (FMV, orthomosaic, and ground survey), pairs of fallen and snapped tree features were manually identified through visual interpretation using the ground survey as a reference. The paired damaged trees feature between FMV and ground survey, and between orthomosaic and ground survey were defined as matched, while non-paired features from the ground survey were defined as unmatched.

Besides, in this study, position accuracy was defined as the distance from the position determined in FMV or orthomosaic to that in the ground survey as explained in detail below. The longer the distance, the lower the position accuracy.

For fallen trees, the visual identification of the pairs was mainly based on the position and angle direction of the fallen trees. I matched pairs between FMV and ground survey, and between orthomosaic and ground survey. For position accuracy, using the ground survey as a reference, the center point for each feature line was determined and the distance between the center points of matched pairs were measured. Besides, the length of matched and unmatched feature lines was also compared.

For snapped trees, the pairs were defined considering the feature data position. I only identified pairs between FMV and ground survey since it was not possible to identify snapped trees from the orthomosaic. For position accuracy, the distance between matched feature points between FMV and the ground survey was measured. Also, the physical characteristics (height and diameter) of matched and unmatched pairs were compared.

To examine the influence of the ground surface on the identification of fallen and snapped trees through FMV and orthomosaic, a 0.25 m buffer was created for each fallen and snapped tree. The buffer size was defined according to Morimoto et al. (2014), where the average trunk diameter in this study area was about 0.5 m. Inside each buffer, the percentage of vegetation with leaves, vegetation without leaves, and non-vegetation were calculated from the classification map generated from the orthomosaic (Figure 27). This was necessary since the vegetation and branches frequently hide fallen and snapped trees when viewed from above (Inoue et al., 2014). To understand the differences in ground surface conditions, between matched and unmatched fallen and snapped trees, the Mann-Whitney U test with a significance level of $P<0.05$ was used.

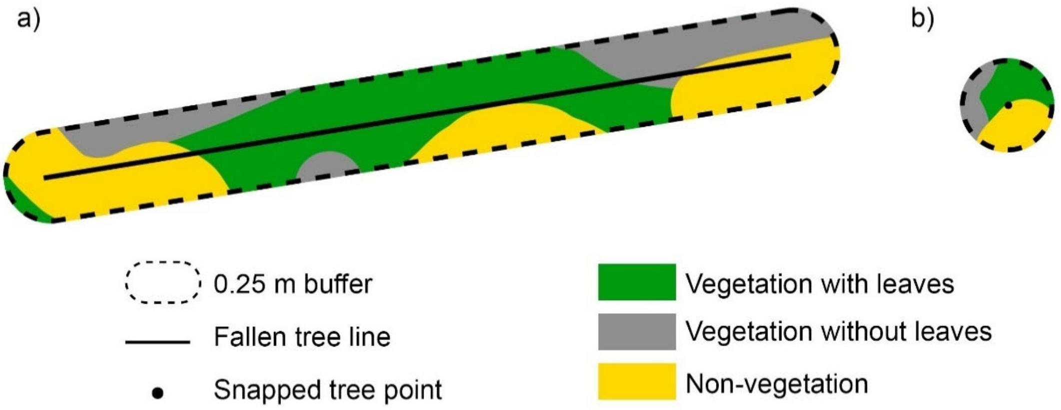

Figure 27. Example of the proportion of vegetation with leaves, vegetation without leaves, and non-vegetation inside a) fallen and b) snapped trees 0.25 m buffer.

4.4 Results

4.4.1 Fallen Trees

Figure 28 showed the matched and unmatched number of fallen trees identified by FMV and ground survey, and by the orthomosaic and ground survey.

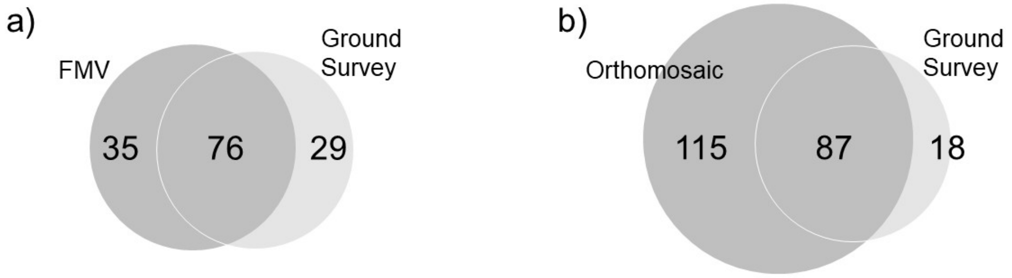

Figure 28. The matched and unmatched number of fallen trees identified by a) FMV and ground survey, and b) orthomosaic and ground survey.

Through FMV, a total of 111 fallen trees were identified, while through orthomosaic and the ground survey a total of 202 and 105 fallen trees were identified respectively. Between the FMV and ground survey, 76 fallen trees were matched, while for non-paired fallen trees, the FMV identified 35, and the ground survey 29 (unmatched). Between the orthomosaic and ground survey, 87 fallen trees were matched, while non-paired fallen trees were 115 and 18 (unmatched) in the orthomosaic and ground survey respectively.

Considering the position accuracy measured through the distance between the center points of each matched pair of fallen trees, the FMV was 2.58 (s.d. 1.88) m on average, while by orthomosaic it was an average of 1.47 (s.d. 1.51) m. Mean lengths of fallen trees including matched and unmatched trees were 10.01 (s.d. 3.33) m, 8.25 (s.d. 3.16) m, and 6.96 (s.d. 3.21) m in the ground survey, FMV, and orthomosaic respectively.

The ground surface condition from matched and unmatched trees (FMV and orthomosaic) are shown in Figure 29, with the respective p-values (Table 7).

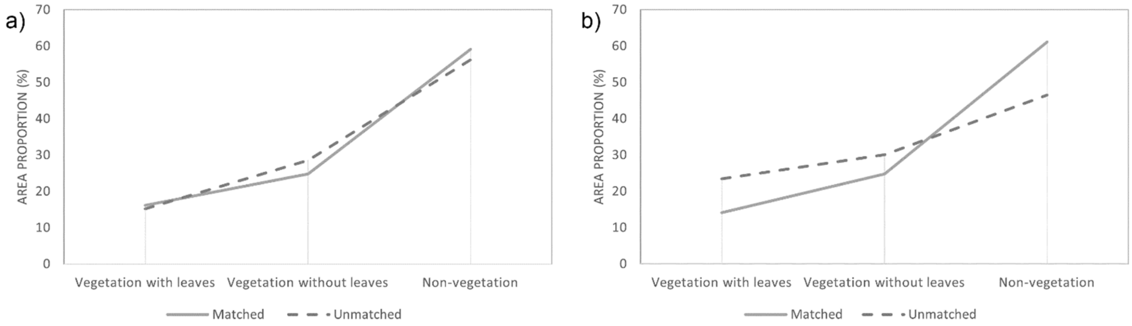

Figure 29. The average proportion of each class inside the buffer of matched and unmatched fallen trees for a) FMV and b) orthomosaic, with the ground survey as reference.

Table 7. P-values between matched and unmatched fallen trees for each class.

	FMV	Orthomosaic
Vegetation with leaves	0.78	0.01
Vegetation without leaves	0.15	0.11
Non-vegetation	0.35	0.002

In general, the results from FMV for matched and unmatched fallen trees were similar in all three classes (Figure 29a) with the p-values showing no significant differences among all three classes (Table 7). For the vegetation with leaves class, the matched and unmatched fallen trees had an average of 16.14 (s.d. 14.4)% and 15.20 (s.d. 13.7)% respectively, while for vegetation without leaves, the results presented an average of 24.77 (s.d. 17.6)% for matched fallen trees and 28.58 (s.d. 14.22)% for unmatched trees. The non-vegetation class had the highest percentage among all three classes, with an average of 59.09 (s.d. 19.07)% for matched fallen trees and 56.22 (s.d. 17.19)% for unmatched fallen trees (Figure 29a).

On the other hand, between the orthomosaic and ground survey, the difference between matched and unmatched fallen trees was higher (Figure 29b). For vegetation with leaves class, while the matched fallen trees presented an average of 14.10 (s.d. 13.36)%, the unmatched fallen trees presented an average of 23.44 (s.d. 15.23) %; the p-value showed that there was a significant difference between matched and unmatched fallen trees. The non-vegetation class also had a significant difference between matched and unmatched fallen trees, but the matched fallen trees average was higher compared to unmatched fallen trees (61.08 (s.d. 17.52) % and 46.47 (s.d. 18.49) % respectively). On the other hand, for the vegetation without leaves class, the matched fallen trees had an average of 24.82 (s.d. 30.09) %, while unmatched fallen trees presented an average of 30.09 (s.d. 14.78) % with the p-value showing no significant difference between matched and unmatched fallen trees.

4.4.2 Snapped Trees

Figure 30 shows only the matched and unmatched number of snapped trees identified by FMV and ground survey. The identification of snapped trees between orthomosaic and ground survey was not possible.

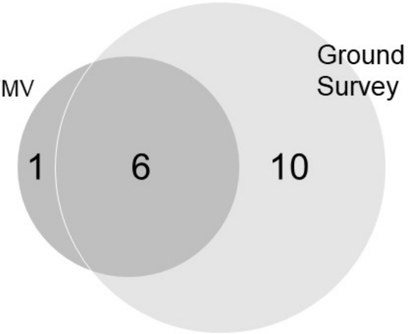

Figure 30. The number of matched and unmatched snapped trees between FMV and ground survey.

Between the FMV and ground survey, 6 snapped trees were matched, while non-paired snapped trees, the FMV identified 1 snapped tree, and the ground survey 10 (unmatched) snapped trees. Considering the ground survey as the reference, the position accuracy of FMV had an average of 2.31 (s.d. 0.61) m.

The physical characteristics of matched and unmatched trees between FMV and ground survey showed higher height averages for matched snapped trees (313.33 (s.d. 175.37) cm) compared to the unmatched snapped trees (149 (s.d. 46.36) cm). For diameter dimensions, the matched snapped trees had an average of 18.17 (s.d. 5.73) cm, while unmatched snapped trees had an average of 11.10 (s.d. 7.37) cm (Figure 31).

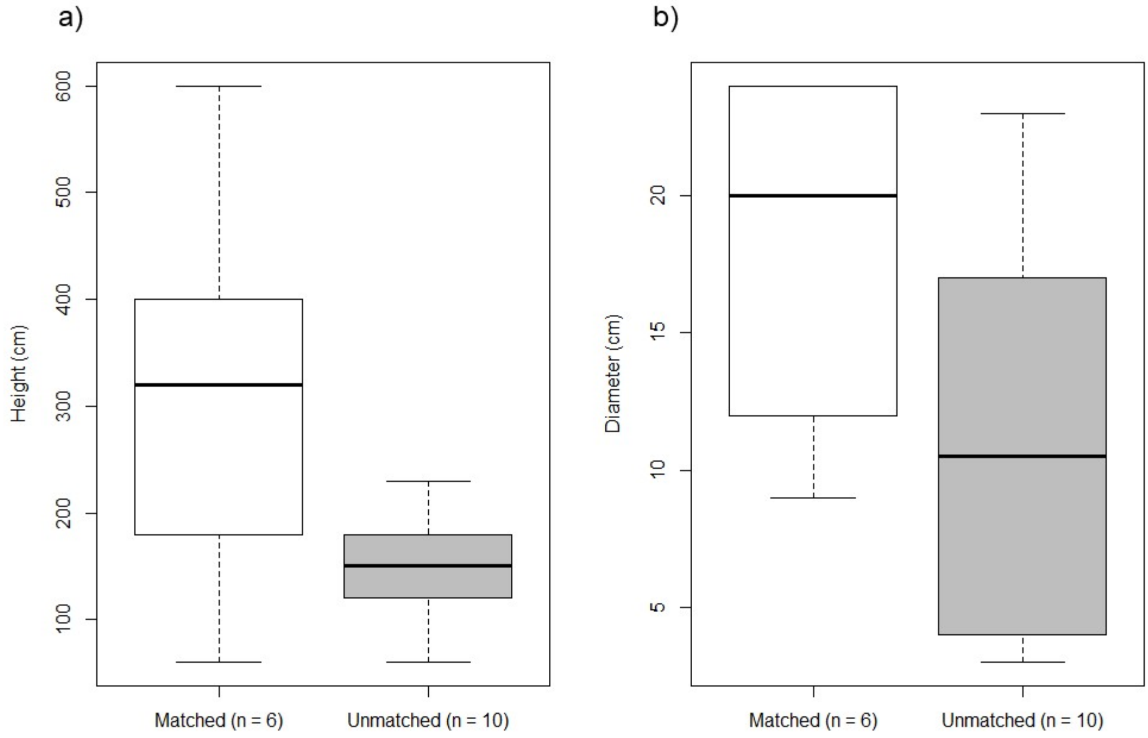

Figure 31. Physical characteristics of snapped trees in cm: a) height and b) diameter.

The coverage proportion of vegetation with leaves, vegetation without leaves, and non-vegetation for FMV is shown in Figure 32, with the respective p-values (Table 8):

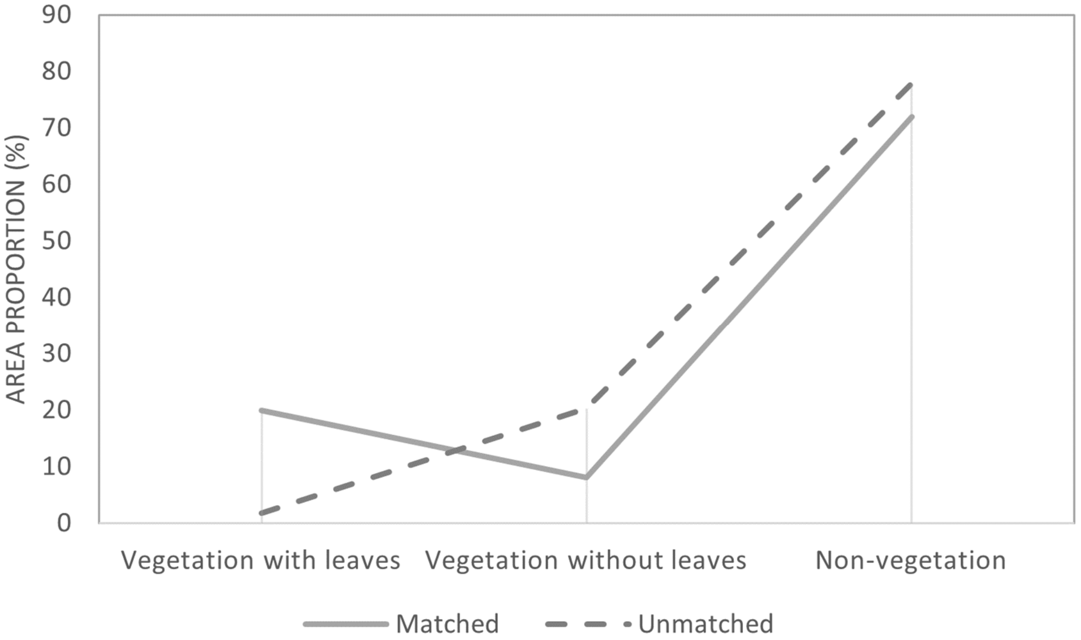

Figure 32. The average proportion of each class inside the buffer of matched and unmatched snapped trees FMV.

Table 8. P-values between matched and unmatched snapped trees for each class.

	FMV
Vegetation with leaves	0.10
Vegetation without leaves	0.83
Non-vegetation	0.33

Because of the small number of samples, the variance between matched and unmatched snapped trees was high. The p-value showed a non-significant difference between matched and unmatched trees. Although looking into the mean values, the vegetation with leaves class had higher average values (19.92 (s.d. 21.7) %) for the matched snapped trees and lower average values (1.84 (s.d. 3.08) %) for unmatched snapped trees. Contrarily to that, the vegetation without leaves class had an average of 8.09 (s.d. 6.79) % for matched snapped trees, and 20.28 (s.d. 28.5) % for unmatched snapped trees. The non-vegetation class was also higher on unmatched snapped trees when compared to the matched snapped trees (77.87 (s.d. 30.86) % and 71.99 (s.d. 23.55) % respectively).

4.5 Discussions

The FMV technology was suitable to identify damaged trees in a windthrow area due to the ability of video to bring better context-awareness. Although delivering lower position accuracies compared to the orthomosaic, the FMV was capable to identify fallen trees even with the presence of vegetation with leaves and vegetation without leaves covering them. The identification of snapped trees was also possible through FMV, opposite to the orthomosaic, which could not identify snapped trees.

4.5.1 Performance of FMV and Orthomosaic for Fallen Trees Identification

In both, FMV and orthomosaic, I found more fallen trees than those in the ground survey (Figure 28). This happened for two main factors: it was possible to survey the whole study area (Lechner et al., 2020), and because of the presence of vegetation with leaves, the orthomosaic identified one single fallen tree as multiple fallen trees (Appendix Figure A3).

For FMV, the graph in Figure 29a showed no differences in the 3 classes between matched and unmatched trees, evidencing that the environment did not have a significant influence on the identification of fallen trees. The camera angle and the different perspectives from the same target throughout the frames helped in the identification of fallen trees even with the presence of vegetation with leaves and vegetation without leaves.

For orthomosaic, the graph in Figure 29b showed a higher difference in vegetation with leaves and non-vegetation classes between matched and unmatched fallen trees compared to FMV. Apart from having fewer non-vegetation averages, the higher amount of vegetation with leaves for unmatched trees showed that the fallen trees were partially or fully covered, where one single fallen tree could be identified as multiple fallen trees (Appendix Figure A3). Thus, resulting in a higher number of fallen trees with a shorter length average, 6.96 (s.d. 3.21) m for orthomosaic compared to 10.01 (s.d. 3.33) m for the ground survey (Appendix Figure A3).

Overall, for fallen trees identification, the ability of video in delivering more context-awareness compared to the orthomosaic (Esri, 2022b; Meisner, 1986) shows the potential of FMV in identifying fallen trees in areas with vegetation coverage, while only visible trees could be identified by orthomosaics (Koi et al., 2022). Although the frame movement delivered better context awareness, it was also a hindrance to identifying fallen trees. Since the frame is always moving, consequently its position is also moving, generating a misalignment between some frames (Lipton et al., 1998). This led to a lower position accuracy when compared to the orthomosaic.

4.5.2 Performance of FMV for Snapped Trees Identification

The ability of FMV to see the same snapped tree in different frames (since the video is moving), made it possible to identify snapped trees through video (Lipton et al., 1998). Although the video movement made it possible to identify snapped trees, the position accuracy of snapped trees was similar to fallen trees' identification accuracy (2.58 (s.d. 1.88) m for fallen trees, and 2.31 (s.d. 0.61) m for snapped trees). This also happened because of the misalignment between video frames which are always moving.

The characteristics of matched snapped trees were taller and thicker compared to unmatched ones (Figure 31), consequently, shorter and thinner snapped trees were assumed to be harder to identify. Physical characteristics were not the only variables to affect their identification, the presence of vegetation without leaves was also a hindrance to the identification of snapped trees due to their similarity with the living tree branches.

The combination of shorter and thinner snapped trees in areas with the presence of vegetation without leaves (branches of deciduous trees) makes snapped trees difficult to be identified in windthrow areas due to the similarity between tree branches and snapped trees. Although higher averages of vegetation with leaves for matched snapped trees, the color difference between the snapped tree and the green vegetation was less of a hindrance to identifying snapped trees (Appendix Figure A4).

4.5.3 FMV Advantages and Limitations for Damaged Trees Identification

While the FMV delivered lower position accuracies compared to the orthomosaic, it can be sufficiently used to calculate the number of damaged trees based on unit per area. Also, since an RTK UAV was used for this study, the data taken from FMV yielded results with better accuracy (around 3 m) than common handheld GNSS devices, which generally variates between 5 to 10 m under favorable conditions (Garmin, 2022). Another limitation of FMV was observed in the identification of short and thin snapped trees, but larger segments of deadwood, which remain longer and play an important role in habitat in forest ecosystems (Lachat et al., 2013), could be identified by using FMV.

Contrarily to the orthomosaic, the FMV was able to identify snapped trees. The FMV showed a simpler workflow and faster processing time compared with the orthomosaic, mainly due to the ability to analyze the data by just combining the metadata with the video. Thus, the FMV method allows quick assessment of individual damaged trees (Jacbos & Eggen-McIntosh, 1993), delivering fast and accurate information to forest managers in order to take quick actions, which is key in deciding the management to be taken on disturbed areas (Dobor et al., 2020; Leverkus et al., 2021). Furthermore, FMV technology also showed great potential to improve and support the interpretation of remote sensed data and ground surveys, due to the enhanced context-awareness provided by the video.

Overall, the FMV showed to be a powerful tool for the disaster management process due to its simple workflow, accurate, and quick results – even with the presence of vegetation - providing detailed information on damaged trees in windthrow areas to identify optimum management measures. New studies using this technology combined with other technologies, such as object detection through deep learning, are encouraged to automatically detect damaged trees in windthrow areas.

CHAPTER 5: GENERAL DISCUSSIONS

5.1 Remote Sensing Approaches to Support for Forest Management After Natural Disturbances

The goal of this thesis was to propose three different approaches to facilitate the implementation of remote sensing to characterize windthrow and landslides on three different scales. Each chapter presented approaches consisting of methods and/or tools to characterize windthrow and landslide on an appropriate scale (Figure 33).

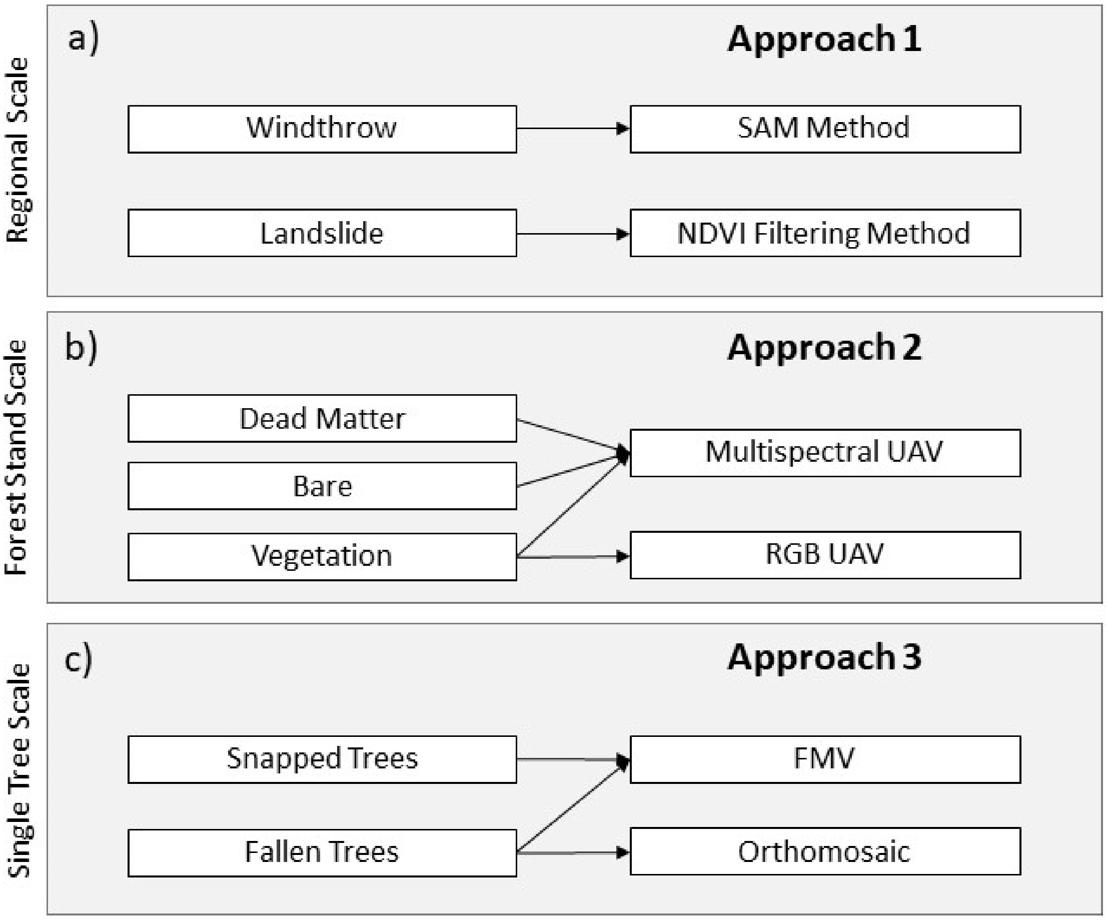

Figure 33. a) The first approach presented appropriate classification methods according to damage type at a regional scale using Planetscope data. b) The second approach presented suitable tools to characterize damaged areas at forest stand scale throughout the months; c) the third approach proposed a methodology based on FMV to identify fallen and snapped trees at a single tree scale in damaged areas.

In Chapter 2, using the Planetscope dataset, the NDVI filtering method showed to be more suitable for landslide identification, while the SAM method was more suitable for windthrow detection. The high availability, low cost, and high spatial resolution of the Planetscope dataset allowed the identification of windthrow and landslide, at a regional scale, right after the natural disturbance. The higher availability of imagery increased the chances of obtaining cloud-free images. Since 2016, the number of Planetscope satellites in orbit continued to increase (European Space Agency, 2022; Gillmore, 2022), and are also improving their capabilities with more spectral bands (Planet Labs Inc., 2022), indicating an important trend in satellite imagery availability and quality, key for disaster management. QGIS and Google Engine also played an important role to apply classification algorithms to interpret the imagery. The ability to use open source platforms and cloud processing allowed the preprocessing and processing of data with relative ease (Congedo, 2016; Gorelick et al., 2017; QGIS Development Team, 2020) since no high-end computers nor high programming skill levels are necessary to process the data. Through these findings, choosing appropriate approaches according to the type of damage is possible in order to quickly and easily identify forest disturbed areas, which is key for disaster management (Joyce et al., 2009).

Recently, UAVs became more accessible in terms of availability and cost, becoming an important tool for disaster management. Chapter 3 showed the usage of RGB and Multispectral UAV to characterize landslide areas through the SfM photogrammetry process at a forest stand scale, allowing a detailed understanding of the vegetation recovery patterns during 4 months in a landslide area. The RGB UAV, more accessible than the multispectral UAV showed great potential to be used to monitor vegetation growth. On the other hand, the Multispectral UAV showed the potential to classify disturbed sites into vegetation, bare soil, and dead matter, due to its higher spectral resolution. Both UAVs allowed monthly monitoring delivering a better understanding of the dynamic process of initial vegetation recovery in landslide areas. This chapter demonstrated the ability of each UAV to characterize landslides over the months at a forest stand scale, supporting forest managers in selecting the appropriate tool to implement remote sensing in the management of disturbed forest areas.

Chapter 4 tested a method based on video taken from a UAV combined with GIS (Esri, 2022b). The proposed approach using FMV was suitable to identify fallen and snapped trees in a windthrow area, mainly due to the ability of video in delivering better context-awareness. Although, it presented lower position accuracy when compared to the orthomosaic, for the same reason which delivered better context-awareness, the video frame movement. The video approach was documented previously (Fang et al., 2008; Jacbos & Eggen-McIntosh, 1993), but the lower resolution and no direct linkage with geospatial data was a hindrance at that time, also requiring high budgets to run video cameras on airplanes. Today, videos taken with high-resolution cameras coupled in commercial UAVs, and the possibility to be combined with the position data provided by the UAV, showed great potential to characterize disturbed forest areas. The context-awareness provided by the video overcoming some of the limitations of the SfM photogrammetry with a less complex preprocessing workflow can be a game-changer for forest managers to monitor disturbed areas at a single tree scale and also to support the interpretation of other types of data.

The results seen in all three chapters can facilitate the implementation of remote sensing at multiple scales, which are important for providing appropriate information according to the scale in a timely manner (Joyce et al., 2009; Woodcock & Strahler, 1987).

5.2 Challenges of Remote Sensing Approaches

Although delivering important information to forest managers, all 3 chapters showed that no single approach is suitable for all applications, Xie et al. (2008) reported similar results. Each approach presented strong and weak points on the regional scale, forest stand scale, and single tree scale. Chapter 2 focused on the regional scale, although the high spatial/temporal resolution and already preprocessed satellite imagery, all three classification methods generated misclassifications. In Chapter 3, although UAVs deliver much higher spatial resolution compared to satellite imagery, the influence of illumination conditions was a challenge in acquiring homogenous data for comparison. The spectral difference between images over the months was a hindrance to understanding the recovery of vegetation.

In Chapter 4, although a better understanding of the limitations of the SfM photogrammetry process and the ability to identify fallen and snapped trees at a single tree scale through FMV, the methodology was based on empirical interpretation of the data. Future studies are recommended in order to automate the identification process. In all 3 chapters, ground data were collected to validate the outputs from the remote sensing. According to Wu et al. (2019), the validation of the remote sensing products is critical for the application of these results in research studies, emphasizing that knowledge in different fields is essential to properly interpret the remotely sensed data (Bernd et al., 2017).

5.3 Future Considerations

As climate change progresses, the need for quick actions to mitigate the damage and create more resilience in forest ecosystems is essential. Based on the premise of availability of data and methods, easiness of use, and cost, the remote sensing technology showed to be ready to be used by non-experts to identify and analyze windthrow and landslide areas on different scales. As shown in this thesis, appropriate approaches can support forest managers to implement remote sensing to characterize windthrow and landslides on different scales.

Remote sensing will continue to develop and play an important role in the forest management field (Abad-Segura et al., 2020). Consequently, research based on facilitating the implementation of remote sensing techniques and training forest managers is essential for forest management after natural disasters.

APPENDIX

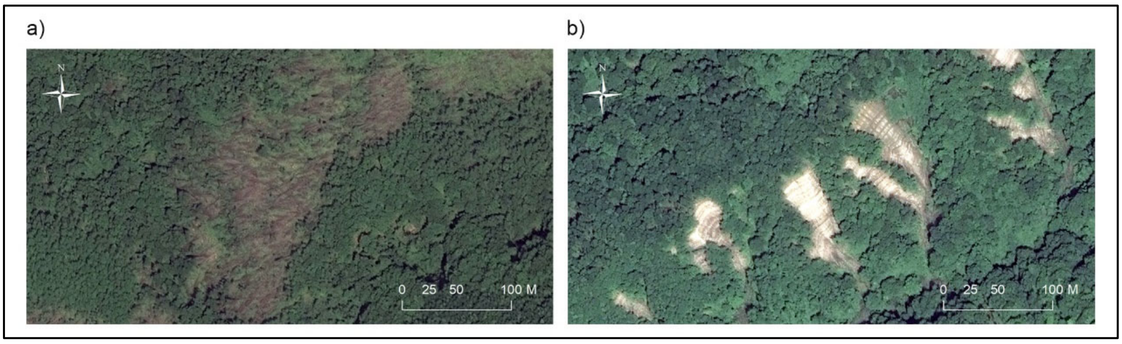

Figure A1. a) Windthrow area and b) landslide areas seen by Worldview 2 imagery used for random points interpretation.

Figure A2. The surveyed area in the ground survey.

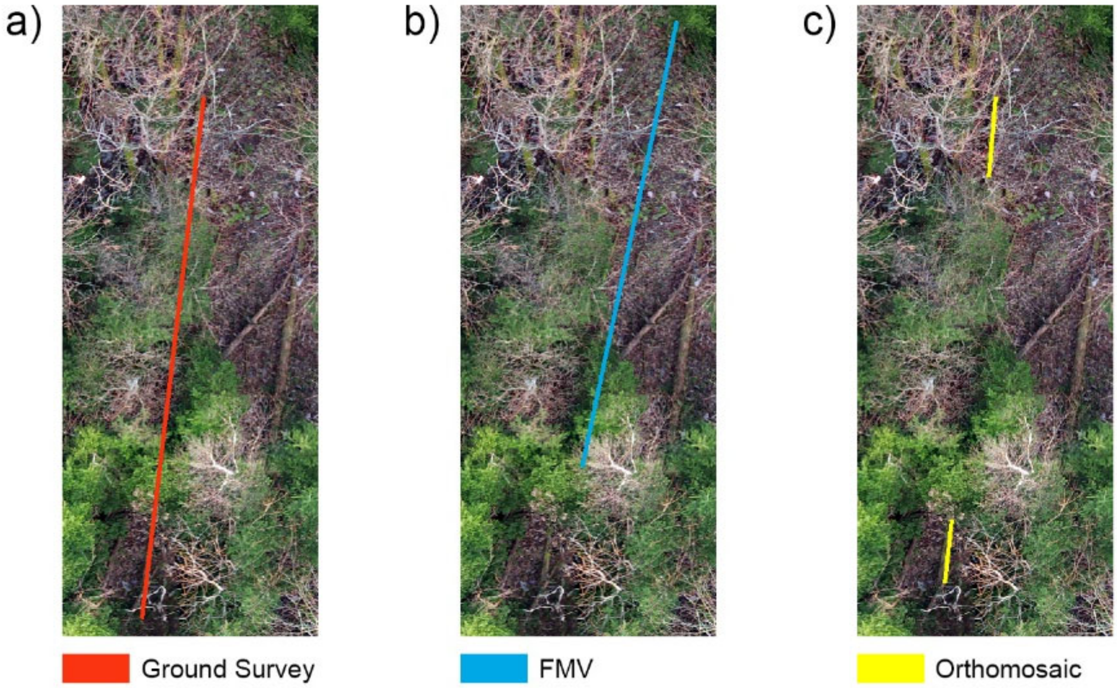

Figure A3. Fallen trees identified through a) ground survey, b) FMV, and c) orthomosaic.

Figure A4. Video frame from a snapped tree.

ACKNOWLEDGMENTS

First and foremost, I want to give my deepest gratitude to God for His blessing throughout my research work.

I would like to express my deep and sincere gratitude to my research supervisor Associate Prof. Dr. Junko Morimoto, Laboratory of Ecosystem Management, Graduate School of Agriculture, Hokkaido University, for giving me the opportunity to do research and providing invaluable guidance and support throughout my research.

In addition to that, I would like to thank Prof. Dr. Futoshi Nakamura; Prof. Dr. Masato Shibuya, Division of Bioresources and Product Science, Graduate School of Agriculture, Hokkaido University; and Associate Prof. Dr. Takashi Koi, Center for Natural Hazards Research, Hokkaido University for giving essential advice to improve my work.

I would also like to thank Prof. Masami Kaneko, Department of Environmental and Symbiotic Science, College of Agriculture, Food and Environmental Sciences, Rakuno Gakuen University, and his team, and Dr. Nobuhiko Yoshimura for supporting my journey in Japan from the beginning.

Very special thanks to my lab mates who helped me in the field surveys and discussions during the years, especially to Hiroaki Ando who supported me in every field survey.

I am extremely grateful to my family for their love, prayers, caring, and sacrifices for educating and preparing me for my future even though being on the other side of the planet.

I am extending my thanks to The Association of Nikkei and Japanese Abroad, JICA, JSPS KAKENHI Grant Number JP17H01516, and the TOUGOU Grant Number JPMXD0717935498 for financially supporting my research throughout the years in Japan. Also, FRS Corporation and Esri for providing tools and Planet Labs Inc. for data providing.

Finally, my thanks go to all people who have supported me to complete my research work directly or indirectly.

REFERENCES

Abad-Segura, E., González-Zamar, M.-D., Vázquez-Cano, E., & López-Meneses, E. (2020). Remote Sensing Applied in Forest Management to Optimize Ecosystem Services: Advances in Research. *Forests*, *11*(9), 969. https://doi.org/10.3390/f11090969

Adler-Golden, S. M., Matthew, M. W., Anderson, G. P., Felde, G. W., & Gardner, J. A. (2002). *Algorithm for de-shadowing spectral imagery* (S. S. Shen (Ed.); p. 203). https://doi.org/10.1117/12.451691

Agisoft Downloads User Manuals. (2019). Agisoft Metashape. https://www.agisoft.com/downloads/user-manuals/

Agisoft Metashape. (2021). https://www.agisoft.com/downloads/installer/

Al-Wassai, F. A., & Kalyankar, N. V. (2013). *Major Limitations of Satellite images*. http://arxiv.org/abs/1307.2434

Alvarez-Vanhard, E., Corpetti, T., & Houet, T. (2021). UAV & satellite synergies for optical remote sensing applications: A literature review. *Science of Remote Sensing*, *3*(October 2020), 100019. https://doi.org/10.1016/j.srs.2021.100019

Bellia, A. F., & Lanfranco, S. (2019). *A Preliminary Assessment of the Efficiency of Using Drones in Land Cover Mapping*. 18–27. https://doi.org/10.7423/XJENZA.2019.1.02

Bernd, A., Braun, D., Ortmann, A., Ulloa-Torrealba, Y. Z., Wohlfart, C., & Bell, A. (2017). More than counting pixels - perspectives on the importance of remote sensing training in ecology and conservation. *Remote Sensing in Ecology and Conservation*, *3*(1), 38–47. https://doi.org/10.1002/rse2.27

Berra, E. F., & Peppa, M. V. (2020). Advances and Challenges of UAV SFM MVS Photogrammetry and Remote Sensing: Short Review. *2020 IEEE Latin American GRSS & ISPRS Remote Sensing Conference (LAGIRS)*, *2020-Janua*, 533–538. https://doi.org/10.1109/LAGIRS48042.2020.9285975

BizStation Corp. (2021). *DG-PRO1RWS RTK W-band gnss receiver*. https://www.bizstation.jp/ja/drogger/dg-pro1rws_index.html

Blaschke, T. (2010). Object based image analysis for remote sensing. *ISPRS Journal of Photogrammetry and Remote Sensing*, *65*(1), 2–16. https://doi.org/10.1016/j.isprsjprs.2009.06.004

Boccardo, P., & Giulio Tonolo, F. (2015). Remote Sensing Role in Emergency Mapping for Disaster Response. In G. Lollino, A. Manconi, F. Guzzetti, M. Culshaw, P. Bobrowsky, & F. Luino (Eds.), *Engineering Geology for Society and Territory - Volume 5* (Vol. 5, pp. 17–24). Springer International Publishing. https://doi.org/10.1007/978-3-319-09048-1_3

Buma, B., & Pawlik, L. (2021). Post-landslide soil and vegetation recovery in a dry, montane system is slow and patchy. *Ecosphere*, *12*(1). https://doi.org/10.1002/ecs2.3346

Carvajal-Ramírez, F., Agüera-Vega, F., & Martínez-Carricondo, P. (2021). Editorial for Special Issue "UAV Photogrammetry and Remote Sensing." *Remote Sensing*, *13*(12), 2327. https://doi.org/10.3390/rs13122327

Casagli, N., Frodella, W., Morelli, S., Tofani, V., Ciampalini, A., Intrieri, E., Raspini, F., Rossi, G., Tanteri, L., & Lu, P. (2017). Spaceborne, UAV and ground-based remote sensing techniques for landslide mapping, monitoring and early warning. *Geoenvironmental Disasters*, *4*(1), 9. https://doi.org/10.1186/s40677-017-0073-1

Chasmer, L. E., Ryerson, R. A., & Coburn, C. A. (2022). Educating the Next Generation of Remote Sensing Specialists: Skills and Industry Needs in a Changing World. *Canadian Journal of Remote Sensing*, *48*(1), 55–70. https://doi.org/10.1080/07038992.2021.1925531

Chećko, E., Jaroszewicz, B., Olejniczak, K., & Kwiatkowska-Falińska, A. J. (2015). The importance of coarse woody debris for vascular plants in temperate mixed deciduous forests. *Canadian Journal of Forest Research*, *45*(9), 1154–1163. https://doi.org/10.1139/cjfr-2014-0473

Chen, W., Li, X., Wang, Y., Chen, G., & Liu, S. (2014). Forested landslide detection using LiDAR data and the random forest algorithm: A case study of the Three Gorges, China. *Remote Sensing of Environment*, *152*, 291–301.

https://doi.org/10.1016/j.rse.2014.07.004

Chiang, L.-C., Lin, Y.-P., Huang, T., Schmeller, D. S., Verburg, P. H., Liu, Y.-L., & Ding, T.-S. (2014). Simulation of ecosystem service responses to multiple disturbances from an earthquake and several typhoons. *Landscape and Urban Planning*, *122*, 41–55. https://doi.org/10.1016/j.landurbplan.2013.10.007

Chirici, G., Bottalico, F., Giannetti, F., Del Perugia, B., Travaglini, D., Nocentini, S., Kutchartt, E., Marchi, E., Foderi, C., Fioravanti, M., Fattorini, L., Bottai, L., McRoberts, R. E., Næsset, E., Corona, P., & Gozzini, B. (2018). Assessing forest windthrow damage using single-date, post-event airborne laser scanning data. *Forestry: An International Journal of Forest Research*, *91*(1), 27–37. https://doi.org/10.1093/forestry/cpx029

Coburn, C. A., Smith, A. M., Logie, G. S., & Kennedy, P. (2018). Radiometric and spectral comparison of inexpensive camera systems used for remote sensing. *International Journal of Remote Sensing*, *39*(15–16), 4869–4890. https://doi.org/10.1080/01431161.2018.1466085

Cohen, J. (1960). A Coefficient of Agreement for Nominal Scales. *Educational and Psychological Measurement*, *20*(1), 37–46. https://doi.org/10.1177/001316446002000104

Congedo, L. (2016). *Semi-Automatic Classification Plugin Documentation. Release 6.0.1.1*. https://doi.org/10.13140/RG.2.2.29474.02242/1

Cooper-Ellis, S., Foster, D. R., Carlton, G., & Lezberg, A. (1999). Forest response to catastrophic wind: Results from an experimental hurricane. *Ecology*, *80*(8), 2683–2696. https://doi.org/10.1890/0012-9658(1999)080[2683:FRTCWR]2.0.CO;2

Cortes, C., & Vapnik, V. (1995). Support-vector networks. *Machine Learning*, *20*(3), 273–297. https://doi.org/10.1007/BF00994018

Dale, V. H., Joyce, L. A., McNulty, S., Neilson, R. P., Ayres, M. P., Flannigan, M. D., Hanson, P. J., Irland, L. C., Lugo, A. E., Peterson, C. J., Simberloff, D., Swanson, F. J., Stocks, B. J., & Wotton, B. M. (2001). Climate Change and Forest Disturbances. *BioScience*, *51*(9), 723. https://doi.org/10.1641/0006-

3568(2001)051[0723:CCAFD]2.0.CO;2

Dandois, J. P., & Ellis, E. C. (2010). Remote Sensing of Vegetation Structure Using Computer Vision. *Remote Sensing*, *2*(4), 1157–1176. https://doi.org/10.3390/rs2041157

Danneels, G., Pirard, E., & Havenith, H.-B. (2007). Automatic landslide detection from remote sensing images using supervised classification methods. *2007 IEEE International Geoscience and Remote Sensing Symposium*, 3014–3017. https://doi.org/10.1109/IGARSS.2007.4423479

Dixon, D. J., Callow, J. N., Duncan, J. M. A., Setterfield, S. A., & Pauli, N. (2021). Satellite prediction of forest flowering phenology. *Remote Sensing of Environment*, *255*, 112197. https://doi.org/10.1016/j.rse.2020.112197

DJI. (2022). *Phantom 4 RTK*. https://www.dji.com/phantom-4-rtk?site=brandsite&from=nav

Dobor, L., Hlásny, T., Rammer, W., Zimová, S., Barka, I., & Seidl, R. (2020). Is salvage logging effectively dampening bark beetle outbreaks and preserving forest carbon stocks? *Journal of Applied Ecology*, *57*(1), 67–76. https://doi.org/10.1111/1365-2664.13518

Dobrinic, D. (2018, June 20). *HORIZONTAL ACCURACY ASSESSMENT OF PLANETSCOPE, RAPIDEYE AND WORLDVIEW-2 SATELLITE IMAGERY*. https://doi.org/10.5593/sgem2018/2.3/S10.017

Donner, A., Shoukri, M. M., Klar, N., & Bartfay, E. (2000). Testing the equality of two dependent kappa statistics. *Statistics in Medicine*, *19*(3), 373–387. https://doi.org/10.1002/(SICI)1097-0258(20000215)19:3<373::AID-SIM337>3.0.CO;2-Y

Duffy, J. P., Cunliffe, A. M., DeBell, L., Sandbrook, C., Wich, S. A., Shutler, J. D., Myers-Smith, I. H., Varela, M. R., & Anderson, K. (2018). Location, location, location: considerations when using lightweight drones in challenging environments. *Remote Sensing in Ecology and Conservation*, *4*(1), 7–19. https://doi.org/10.1002/rse2.58

Duncan, R. P. (1993). Flood Disturbance and the Coexistence of Species in a Lowland Podocarp Forest, South Westland, New Zealand. *The Journal of Ecology*, *81*(3), 403. https://doi.org/10.2307/2261519

Einzmann, K., Immitzer, M., Böck, S., Bauer, O., Schmitt, A., & Atzberger, C. (2017). Windthrow Detection in European Forests with Very High-Resolution Optical Data. *Forests*, *8*(1), 21. https://doi.org/10.3390/f8010021

Esri. (2022a). *ArcGIS Pro*. https://www.esri.com/en-us/arcgis/products/arcgis-pro/overview

Esri. (2022b). *Introduction to Full Motion Video*. https://pro.arcgis.com/en/pro-app/2.7/help/analysis/image-analyst/introduction-to-full-motion-video-in-arcgis-pro.htm

Esri. (2022c). *Site Scan for ArcGIS*. https://www.esri.com/en-us/arcgis/products/site-scan-for-arcgis/overview

European Space Agency. (2022). *PlanetScope - Mission Background*. https://earth.esa.int/eogateway/missions/planetscope/description#:~:text=Mission Background&text=130%2B DOVES from PlanetScope have,satellites on 14 July 2017

Fang, L., Xu, A., & Tang, L. (2008). A Study of the Key Technology of Forest Fire Prevention Based on a Cooperation of Video Monitor and GIS. *2008 Fourth International Conference on Natural Computation*, *5*, 391–396. https://doi.org/10.1109/ICNC.2008.428

Feng, Y., & Wang, J. (2008). GPS RTK Performance Characteristics and Analysis. *Journal of Global Positioning Systems*, *7*(1), 1–8. https://doi.org/10.5081/jgps.7.1.1

Foody, G. M. (2004). Thematic Map Comparison. *Photogrammetric Engineering & Remote Sensing*, *70*(5), 627–633. https://doi.org/10.14358/PERS.70.5.627

Forest Management Division, Bureau of Forestry, Department of Fisheries and Forestry, H. G. (2018). *Forest Management to Reduce the Risk of Damage of Windthrow*. http://www.pref.hokkaido.lg.jp/sr/srs/riskdown.pdf

Fuentes-Peailillo, F., Ortega-Farias, S., Rivera, M., Bardeen, M., & Moreno, M. (2018). Comparison of vegetation indices acquired from RGB and Multispectral sensors placed on UAV. *2018 IEEE International Conference on Automation/XXIII Congress of the Chilean Association of Automatic Control (ICA-ACCA)*, 1–6. https://doi.org/10.1109/ICA-ACCA.2018.8609861

Furukawa, F., Laneng, L. A., Ando, H., Yoshimura, N., Kaneko, M., & Morimoto, J. (2021). Comparison of RGB and Multispectral Unmanned Aerial Vehicle for Monitoring Vegetation Coverage Changes on a Landslide Area. *Drones*, *5*(3), 97. https://doi.org/10.3390/drones5030097

Furukawa, F., Morimoto, J., Yoshimura, N., & Kaneko, M. (2020). Comparison of Conventional Change Detection Methodologies Using High-Resolution Imagery to Find Forest Damage Caused by Typhoons. *Remote Sensing*, *12*(19), 3242. https://doi.org/10.3390/rs12193242

Garmin. (2022). *GPS Accuracy*.

Geospatial Intelligence Standards Working Group. (2022). *NSG Standards Registry*. https://nsgreg.nga.mil/doc/view?i=5093

Gillmore, C. (2022). *Planet To Launch 44 SuperDove Satellites On SpaceX's Falcon 9 Rocket*. https://www.planet.com/pulse/planet-to-launch-44-superdove-satellites-on-spacexs-falcon-9-rocket/

Giri, C. (2016). Observation and Monitoring of Mangrove Forests Using Remote Sensing: Opportunities and Challenges. *Remote Sensing*, *8*(9), 783. https://doi.org/10.3390/rs8090783

Gomez, C., & Purdie, H. (2016). UAV- based Photogrammetry and Geocomputing for Hazards and Disaster Risk Monitoring – A Review. *Geoenvironmental Disasters*, *3*(1), 23. https://doi.org/10.1186/s40677-016-0060-y

Gorelick, N., Hancher, M., Dixon, M., Ilyushchenko, S., Thau, D., & Moore, R. (2017). Google Earth Engine: Planetary-scale geospatial analysis for everyone. *Remote Sensing of Environment*, *202*, 18–27. https://doi.org/10.1016/j.rse.2017.06.031

Guariguata, M. R. (1990). Landslide Disturbance and Forest Regeneration in the Upper Luquillo Mountains of Puerto Rico. *The Journal of Ecology*, *78*(3), 814. https://doi.org/10.2307/2260901

Gülch, E., Al-Ghorani, N., Quedenfeldt, B., & Braun, J. (2012). EVALUATION AND DEVELOPMENT OF E-LEARNING TOOLS AND METHODS IN DIGITAL PHOTOGRAMMETRY AND REMOTE SENSING FOR NON EXPERTS FROM ACADEMIA AND INDUSTRY. *The International Archives of the Photogrammetry, Remote Sensing and Spatial Information Sciences*, *XXXIX-B6*, 1–6. https://doi.org/10.5194/isprsarchives-XXXIX-B6-1-2012

Habib, a F., Ghanma, M. S., & Tait, M. (2004). Integration of Lidar and Photogrammetry for Close Range Applications. *International Archives of Photogrammetry, Remote Sensing and Spatial Information Sciences*, 170. http://citeseerx.ist.psu.edu/viewdoc/download?doi=10.1.1.80.3895&rep=rep1&type=pdf

Hall, F. G., Strebel, D. E., Nickeson, J. E., & Goetz, S. J. (1991). Radiometric rectification: Toward a common radiometric response among multidate, multisensor images. *Remote Sensing of Environment*, *35*(1), 11–27. https://doi.org/10.1016/0034-4257(91)90062-B

Hamdi, Z. M., Brandmeier, M., & Straub, C. (2019). Forest Damage Assessment Using Deep Learning on High Resolution Remote Sensing Data. *Remote Sensing*, *11*(17), 1976. https://doi.org/10.3390/rs11171976

Hansen, M. C., & Loveland, T. R. (2012). A review of large area monitoring of land cover change using Landsat data. *Remote Sensing of Environment*, *122*, 66–74. https://doi.org/10.1016/j.rse.2011.08.024

Hartung, C., Lerer, A., Anokwa, Y., Tseng, C., Brunette, W., & Borriello, G. (2010). Open data kit. *Proceedings of the 4th ACM/IEEE International Conference on Information and Communication Technologies and Development - ICTD '10*, 1–12. https://doi.org/10.1145/2369220.2369236

Heinselman, M. L. (1973). Fire in the virgin forests of the Boundary Waters Canoe Area, Minnesota. *Quaternary Research*, *3*(3), 329–382. https://doi.org/10.1016/0033-5894(73)90003-3

Hervás, J., Barredo, J. I., Rosin, P. L., Pasuto, A., Mantovani, F., & Silvano, S. (2003). Monitoring landslides from optical remotely sensed imagery: the case history of Tessina landslide, Italy. *Geomorphology*, *54*(1–2), 63–75. https://doi.org/10.1016/S0169-555X(03)00056-4

Hirata, Y., Tabuchi, R., Patanaponpaiboon, P., Poungparn, S., Yoneda, R., & Fujioka, Y. (2014). Estimation of aboveground biomass in mangrove forests using high-resolution satellite data. *Journal of Forest Research*, *19*(1), 34–41. https://doi.org/10.1007/s10310-013-0402-5

Hsu, C.-W., Chang, C.-C., & Lin, C.-J. (2008). A Practical Guide to Support Vector Classification. *BJU International*, *101*(11), 1396–1400.

Iglhaut, J., Cabo, C., Puliti, S., Piermattei, L., O'Connor, J., & Rosette, J. (2019). Structure from Motion Photogrammetry in Forestry: a Review. *Current Forestry Reports*, *5*(3), 155–168. https://doi.org/10.1007/s40725-019-00094-3

Im, J., Park, H., & Takeuchi, W. (2019). Advances in Remote Sensing-Based Disaster Monitoring and Assessment. *Remote Sensing*, *11*(18), 2181. https://doi.org/10.3390/rs11182181

Inoue, T., Nagai, S., Yamashita, S., Fadaei, H., Ishii, R., Okabe, K., Taki, H., Honda, Y., Kajiwara, K., & Suzuki, R. (2014). Unmanned aerial survey of fallen trees in a deciduous broadleaved forest in eastern Japan. *PLoS ONE*, *9*(10), 1–7. https://doi.org/10.1371/journal.pone.0109881

Ivanescu, A. E., Li, P., George, B., Brown, A. W., Keith, S. W., Raju, D., & Allison, D. B. (2016). The importance of prediction model validation and assessment in obesity and nutrition research. *International Journal of Obesity*, *40*(6), 887–894. https://doi.org/10.1038/ijo.2015.214

Jacbos, D. M., & Eggen-McIntosh, S. (1993). AIRBORNE VIDEOGRAPHY AND GPS FOR ASSESSMENT OF FOREST DAMAGE IN SOUTHERN LOUISIANA FROM HURRICANE ANDREW. *Proceedings of the ILJFRO Conference on*

Inventory and Management Techniques in the Context of Catastrophic Events, 12.

Japan Meteorological Agency. (2017). *Disaster Meteorological Report - Heavy Rain and Storms from 2016 August 16 to August 31 due to Typhoon No. 7, No. 9, No. 10, No. 11 and Front Line in 2016*.

Japan Meteorological Agency. (2018). *Information on the 2018 Hokkaido Eastern Iburi Earthquake*. http://www.jma.go.jp/jma/menu/20180906_iburi_jishin_menu.html

Japan Meteorological Agency. (2021a). https://www.data.jma.go.jp/obd/stats/etrn/view/hourly_a1.php?prec_no=21&block_no=0124&year=2021&month=7&day=8&view=

Japan Meteorological Agency. (2021b). https://www.data.jma.go.jp/obd/stats/etrn/view/hourly_a1.php?prec_no=21&block_no=0124&year=2021&month=4&day=13&view=

Japanese Ministry of Land Infrastructure Transport and Tourism. (2020). *National Land Numerical Information Download Service*. https://nlftp.mlit.go.jp/ksj/index.html

Jianyaa, G., Haiganga, S., Guoruia, M., & Qimingb, Z. (2008). *A REVIEW OF MULTI-TEMPORAL REMOTE SENSING DATA CHANGE DETECTION ALGORITHMS*.

Jonsson, B., Kruys, N., & Ranius, T. (2005). Ecology of species living on dead wood – lessons for dead wood management. *Silva Fennica*, *39*(2), 289–309. https://doi.org/10.14214/sf.390

Joyce, K. E., Belliss, S. E., Samsonov, S. V., McNeill, S. J., & Glassey, P. J. (2009). A review of the status of satellite remote sensing and image processing techniques for mapping natural hazards and disasters. *Progress in Physical Geography: Earth and Environment*, *33*(2), 183–207. https://doi.org/10.1177/0309133309339563

Joyce, K. E., Wright, K. C., Samsonov, S. V., & Ambrosia, V. G. (2009). Remote sensing and the disaster management cycle. In *Advances in Geoscience and Remote Sensing* (Issue January 2014). InTech. https://doi.org/10.5772/8341

Kalantar, B., Mansor, S. Bin, Sameen, M. I., Pradhan, B., & Shafri, H. Z. M. (2017). Drone-based land-cover mapping using a fuzzy unordered rule induction algorithm integrated into object-based image analysis. *International Journal of Remote Sensing*, *38*(8–10), 2535–2556. https://doi.org/10.1080/01431161.2016.1277043

Kangas, A., & Maltamo, M. (2006). *Forest Inventory* (A. Kangas & M. Maltamo (Eds.); Vol. 10). Springer Netherlands. https://doi.org/10.1007/1-4020-4381-3

Klemas, V. V. (2009). The Role of Remote Sensing in Predicting and Determining Coastal Storm Impacts. *Journal of Coastal Research*, *256*(6), 1264–1275. https://doi.org/10.2112/08-1146.1

Koi, T., Hotta, N., Tanaka, Y., & Katsura, S. (2022). Generation and Subsequent Transport of Landslide-driven Large Woody Debris Induced by the 2018 Hokkaido Eastern Iburi Earthquake. *Frontiers in Earth Science*, *9*. https://doi.org/10.3389/feart.2021.769061

Kruse, F. A., Lefkoff, A. B., Boardman, J. W., Heidebrecht, K. B., Shapiro, A. T., Barloon, P. J., & Goetz, A. F. H. (1993). The spectral image processing system (SIPS)-interactive visualization and analysis of imaging spectrometer data. *AIP Conference Proceedings*, *283*(January 1992), 192–201. https://doi.org/10.1063/1.44433

Kulakowski, D., Seidl, R., Holeksa, J., Kuuluvainen, T., Nagel, T. A., Panayotov, M., Svoboda, M., Thorn, S., Vacchiano, G., Whitlock, C., Wohlgemuth, T., & Bebi, P. (2017). A walk on the wild side: Disturbance dynamics and the conservation and management of European mountain forest ecosystems. *Forest Ecology and Management*, *388*, 120–131. https://doi.org/10.1016/j.foreco.2016.07.037

Kupfer, J. A., & Emerson, C. W. (2005). Remote Sensing. In *Encyclopedia of Social Measurement* (Vol. 3, pp. 377–383). Elsevier. https://doi.org/10.1016/B0-12-369398-5/00340-6

Lachat, T., Bouget, C., Bütler, R., Müller, J., Kraus, D., & Krumm, F. (2013). Deadwood: quantitative and qualitative requirements for the conservation of saproxylic biodiversity. In *Integrative approaches as an opportunity for the conservation of forest biodiversity* (Issue May 2016, pp. 92–102).

Landis, J. R., & Koch, G. G. (1977). An Application of Hierarchical Kappa-type Statistics in the Assessment of Majority Agreement among Multiple Observers. *Biometrics*, *33*(2), 363. https://doi.org/10.2307/2529786

Langner, A., Titin, J., & Kitayama, K. (2012). *The Application of Satellite Remote Sensing for Classifying Forest Degradation and Deriving Above-Ground Biomass Estimates* (K. Kitayama (Ed.); pp. 23–40). Springer Japan. https://doi.org/10.1007/978-4-431-54141-7_2

Lazzeri, G., Frodella, W., Rossi, G., & Moretti, S. (2021). Multitemporal mapping of post-fire land cover using multiplatform prisma hyperspectral and sentinel-uav multispectral data: Insights from case studies in Portugal and Italy. *Sensors*, *21*(12). https://doi.org/10.3390/s21123982

Lechner, A. M., Foody, G. M., & Boyd, D. S. (2020). Applications in Remote Sensing to Forest Ecology and Management. *One Earth*, *2*(5), 405–412. https://doi.org/10.1016/j.oneear.2020.05.001

Leduc, A., Bernier, P. Y., Mansuy, N., Raulier, F., Gauthier, S., & Bergeron, Y. (2015). Using salvage logging and tolerance to risk to reduce the impact of forest fires on timber supply calculations. *Canadian Journal of Forest Research*, *45*(4), 480–486. https://doi.org/10.1139/cjfr-2014-0434

Leverkus, A. B., Buma, B., Wagenbrenner, J., Burton, P. J., Lingua, E., Marzano, R., & Thorn, S. (2021). Tamm review: Does salvage logging mitigate subsequent forest disturbances? *Forest Ecology and Management*, *481*(August 2020), 118721. https://doi.org/10.1016/j.foreco.2020.118721

Lin, C.-Y., Lo, H.-M., Chou, W.-C., & Lin, W.-T. (2004). Vegetation recovery assessment at the Jou-Jou Mountain landslide area caused by the 921 Earthquake in Central Taiwan. *Ecological Modelling*, *176*(1–2), 75–81. https://doi.org/10.1016/j.ecolmodel.2003.12.037

Lipton, A. J., Fujiyoshi, H., & Patil, R. S. (1998). Moving target classification and tracking from real-time video. *Proceedings Fourth IEEE Workshop on Applications of Computer Vision. WACV'98 (Cat. No.98EX201)*, *1998-Octob*, 8–14. https://doi.org/10.1109/ACV.1998.732851

Llano, X. C. (2019). *AcATaMa - QGIS plugin for Accuracy Assessment of Thematic Maps,* *version 19.11*. https://smbyc.github.io/AcATaMa

Lucieer, A., Jong, S. M. d., & Turner, D. (2014). Mapping landslide displacements using Structure from Motion (SfM) and image correlation of multi-temporal UAV photography. *Progress in Physical Geography*, *38*(1), 97–116. https://doi.org/10.1177/0309133313515293

Mabry, C. M., Hamburg, S. P., Lin, T.-C., Horng, F.-W., King, H.-B., & Hsia, Y.-J. (1998). Typhoon Disturbance and Stand-level Damage Patterns at a Subtropical Forest in Taiwan1. *Biotropica*, *30*(2), 238–250. https://doi.org/10.1111/j.1744-7429.1998.tb00058.x

Martha, T. R., Kerle, N., van Westen, C. J., Jetten, V., & Vinod Kumar, K. (2012). Object-oriented analysis of multi-temporal panchromatic images for creation of historical landslide inventories. *ISPRS Journal of Photogrammetry and Remote Sensing*, *67*(1), 105–119. https://doi.org/10.1016/j.isprsjprs.2011.11.004

Martinez, J. L., Lucas-Borja, M. E., Plaza-Alvarez, P. A., Denisi, P., Moreno, M. A., Hernández, D., González-Romero, J., & Zema, D. A. (2021). Comparison of Satellite and Drone-Based Images at Two Spatial Scales to Evaluate Vegetation Regeneration after Post-Fire Treatments in a Mediterranean Forest. *Applied Sciences*, *11*(12), 5423. https://doi.org/10.3390/app11125423

Maxar Technologies. (2020). *WORLDVIEW-2*. https://www.maxar.com/constellation

Maxar Technologies. (2021). *MAXAR - CONSTELLATION*. https://www.maxar.com/constellation

Meisner, D. (1986). Fundamentals of airborne video remote sensing. *Remote Sensing of Environment*, *19*(1), 63–79. https://doi.org/10.1016/0034-4257(86)90041-6

Messina, G., & Modica, G. (2020). Applications of UAV thermal imagery in precision agriculture: State of the art and future research outlook. *Remote Sensing*, *12*(9). https://doi.org/10.3390/RS12091491

Mitchell, P. J., Downie, A.-L., & Diesing, M. (2018). How good is my map? A tool for semi-automated thematic mapping and spatially explicit confidence assessment.

Environmental Modelling & Software, *108*, 111–122. https://doi.org/10.1016/j.envsoft.2018.07.014

MOD09GQ v006. (2021). https://doi.org/10.5067/MODIS/MOD09GQ.006

Mohd Daud, S. M. S., Mohd Yusof, M. Y. P., Heo, C. C., Khoo, L. S., Chainchel Singh, M. K., Mahmood, M. S., & Nawawi, H. (2022). Applications of drone in disaster management: A scoping review. *Science & Justice*, *62*(1), 30–42. https://doi.org/10.1016/j.scijus.2021.11.002

Mokroš, M., Výbošťok, J., Merganič, J., Hollaus, M., Barton, I., Koreň, M., Tomaštík, J., & Čerňava, J. (2017). Early Stage Forest Windthrow Estimation Based on Unmanned Aircraft System Imagery. *Forests*, *8*(9), 306. https://doi.org/10.3390/f8090306

Mori, A. S., Lertzman, K. P., & Gustafsson, L. (2017). Biodiversity and ecosystem services in forest ecosystems: a research agenda for applied forest ecology. *Journal of Applied Ecology*, *54*(1), 12–27. https://doi.org/10.1111/1365-2664.12669

Morimoto, J., Kajihara, K., & Shida, Y. (2014). Environment and plant regeneration at microsites created by fallen logs in plantation forests downed by wind. *Journal of the Japanese Society of Revegetation Technology*, *40*(1), 124–129. https://doi.org/10.7211/jjsrt.40.124

Morimoto, J., Morimoto, M., & Nakamura, F. (2011). Initial vegetation recovery following a blowdown of a conifer plantation in monsoonal East Asia: Impacts of legacy retention, salvaging, site preparation, and weeding. *Forest Ecology and Management*, *261*(8), 1353–1361. https://doi.org/10.1016/j.foreco.2011.01.015

Morimoto, J., & Negishi, J. (2019). Ecological resilience of ecosystems to human impacts: resilience of plants and animals. *Landscape and Ecological Engineering*, *15*(2), 131–132. https://doi.org/10.1007/s11355-019-00376-9

Morimoto, J., Sugiura, M., Morimoto, M., & Nakamura, F. (2021). Restoration of Natural Forests After Severe Wind Disturbance in a Cold, Snowy Region With a Deer Population: Implications From 15 Years of Field Experiments. *Frontiers in Forests and Global Change*, *4*(July), 1–11. https://doi.org/10.3389/ffgc.2021.675475

Morimoto, J., Umebayashi, T., Suzuki, S. N., Owari, T., Nishimura, N., Ishibashi, S., Shibuya, M., & Hara, T. (2019). Long-term effects of salvage logging after a catastrophic wind disturbance on forest structure in northern Japan. *Landscape and Ecological Engineering*, *15*(2), 133–141. https://doi.org/10.1007/s11355-019-00375-w

Mosier, C. I. (1951). I. Problems and Designs of Cross-Validation 1. *Educational and Psychological Measurement*, *11*(1), 5–11. https://doi.org/10.1177/001316445101100101

Mountrakis, G., Im, J., & Ogole, C. (2011). Support vector machines in remote sensing: A review. *ISPRS Journal of Photogrammetry and Remote Sensing*, *66*(3), 247–259. https://doi.org/10.1016/j.isprsjprs.2010.11.001

Murakami, H., Wang, Y., Yoshimura, H., Mizuta, R., Sugi, M., Shindo, E., Adachi, Y., Yukimoto, S., Hosaka, M., Kusunoki, S., Ose, T., & Kitoh, A. (2012). Future Changes in Tropical Cyclone Activity Projected by the New High-Resolution MRI-AGCM. *Journal of Climate*, *25*(9), 3237–3260. https://doi.org/10.1175/JCLI-D-11-00415.1

Narukawa, Y., Iida, S., Tanouchi, H., Abe, S., & Yamamoto, S.-I. (2003). State of fallen logs and the occurrence of conifer seedlings and saplings in boreal and subalpine old-growth forests in Japan. *Ecological Research*, *18*(3), 267–277. https://doi.org/10.1046/j.1440-1703.2003.00553.x

Okamoto, K., & Fukuhara, M. (1996). Estimation of paddy field area using the area ratio of categories in each mixel of Landsat TM. *International Journal of Remote Sensing*, *17*(9), 1735–1749. https://doi.org/10.1080/01431169608948736

Olofsson, P., Foody, G. M., Stehman, S. V., & Woodcock, C. E. (2013). Making better use of accuracy data in land change studies: Estimating accuracy and area and quantifying uncertainty using stratified estimation. *Remote Sensing of Environment*, *129*(16), 122–131. https://doi.org/10.1016/j.rse.2012.10.031

Osanai, N., Yamada, T., Hayashi, S., Kastura, S., Furuichi, T., Yanai, S., Murakami, Y., Miyazaki, T., Tanioka, Y., Takiguchi, S., & Miyazaki, M. (2019). Characteristics of landslides caused by the 2018 Hokkaido Eastern Iburi Earthquake. *Landslides*, *16*(8), 1517–1528. https://doi.org/10.1007/s10346-019-01206-7

Pang, C., Ma, X. K., Lo, J. P., Hung, T. T., & Hau, B. C. (2018). Vegetation succession on landslides in Hong Kong: Plant regeneration, survivorship and constraints to restoration. *Global Ecology and Conservation*, *15*, e00428. https://doi.org/10.1016/j.gecco.2018.e00428

Petropoulos, G. P., Vadrevu, K. P., & Kalaitzidis, C. (2013). Spectral angle mapper and object-based classification combined with hyperspectral remote sensing imagery for obtaining land use/cover mapping in a Mediterranean region. *Geocarto International*, *28*(2), 114–129. https://doi.org/10.1080/10106049.2012.668950

Planet Labs Inc. (2020). *PLANET IMAGERY AND ARCHIVE*.

Planet Labs Inc. (2022). *Planet Launches Next Generation PlanetScope With Eight Spectral Bands And Quality Improvements*. https://www.planet.com/pulse/planet-launches-next-generation-planetscope-with-eight-spectral-bands-and-quality-improvements

QGIS Development Team. (2020). *QGIS Geographic Information System 2009*. https://qgis.org/en/site/

Remondino, F., Barazzetti, L., Nex, F., Scaioni, M., & Sarazzi, D. (2012). UAV PHOTOGRAMMETRY FOR MAPPING AND 3D MODELING – CURRENT STATUS AND FUTURE PERSPECTIVES. *The International Archives of the Photogrammetry, Remote Sensing and Spatial Information Sciences*, *XXXVIII-1/*, 25–31. https://doi.org/10.5194/isprsarchives-XXXVIII-1-C22-25-2011

RETSCHER, G. (2002). Accuracy Performance of Virtual Reference Station (VRS) Networks. *Journal of Global Positioning Systems*, *1*(1), 40–47. https://doi.org/10.5081/jgps.1.1.40

Rossi, G., Nocentini, M., Lombardi, L., Vannocci, P., Tanteri, L., Dotta, G., Bicocchi, G., Scaduto, G., Salvatici, T., Tofani, V., Moretti, S., & Casagli, N. (2016). Integration of multicopter drone measurements and ground-based data for landslide monitoring. In *Landslides and Engineered Slopes. Experience, Theory and Practice* (pp. 1745–

1750). CRC Press. https://doi.org/10.1201/b21520-217

Rossi, G., Tanteri, L., Tofani, V., Vannocci, P., Moretti, S., & Casagli, N. (2018). Multitemporal UAV surveys for landslide mapping and characterization. *Landslides*, *15*(5), 1045–1052. https://doi.org/10.1007/s10346-018-0978-0

Rothmund, S., Vouillamoz, N., & Joswig, M. (2017). Mapping slow-moving alpine landslides by UAV — Opportunities and limitations. *The Leading Edge*, *36*(7), 571–579. https://doi.org/10.1190/tle36070571.1

Rouse, J. W., Hass, R. H., Schell, J. A., & Deering, D. W. (1973). Monitoring vegetation systems in the great plains with ERTS. *Third Earth Resources Technology Satellite (ERTS) Symposium*, *1*, 309–317. https://doi.org/citeulike-article-id:12009708

Rozenstein, O., & Karnieli, A. (2011). Comparison of methods for land-use classification incorporating remote sensing and GIS inputs. *Applied Geography*, *31*(2), 533–544. https://doi.org/10.1016/j.apgeog.2010.11.006

Ruwaimana, M., Satyanarayana, B., Otero, V., M. Muslim, A., Syafiq A., M., Ibrahim, S., Raymaekers, D., Koedam, N., & Dahdouh-Guebas, F. (2018). The advantages of using drones over space-borne imagery in the mapping of mangrove forests. *PLOS ONE*, *13*(7), e0200288. https://doi.org/10.1371/journal.pone.0200288

Rwanga, S. S., & Ndambuki, J. M. (2017). Accuracy Assessment of Land Use/Land Cover Classification Using Remote Sensing and GIS. *International Journal of Geosciences*, *08*(04), 611–622. https://doi.org/10.4236/ijg.2017.84033

Schweik, C. M., & Thomas, C. W. (2002). *Using Remote Sensing to Evaluate Environmental Institutional Designs : A Habitat Conservation Planning Example*. *83*(1). https://doi.org/10.1111/1540-6237.00081

Seidl, R., Thom, D., Kautz, M., Martin-Benito, D., Peltoniemi, M., Vacchiano, G., Wild, J., Ascoli, D., Petr, M., Honkaniemi, J., Lexer, M. J., Trotsiuk, V., Mairota, P., Svoboda, M., Fabrika, M., Nagel, T. A., & Reyer, C. P. O. (2017). Forest disturbances under climate change. *Nature Climate Change*, *7*(6), 395–402. https://doi.org/10.1038/nclimate3303

Sharma, V., Baruah, D., Chutia, D., Raju, P., & Bhattacharya, D. K. (2016). An assessment of support vector machine kernel parameters using remotely sensed satellite data. *2016 IEEE International Conference on Recent Trends in Electronics, Information & Communication Technology (RTEICT)*, *May*, 1567–1570. https://doi.org/10.1109/RTEICT.2016.7808096

Shiels, A. B., Walker, L. R., & Thompson, D. B. (2006). Organic matter inputs create variable resource patches on Puerto Rican landslides. *Plant Ecology*, *184*(2), 223–236. https://doi.org/10.1007/s11258-005-9067-2

Siitonen, J. (2001). Forest Management, Coarse Woody Debris and Saproxylic Organisms: Fennoscandian Boreal Forests as an Example. *Ecological Bulletins, Ecology of Woody Debris in Boreal Forests*, *49*, 11–41. https://doi.org/10.2307/20113262

Softbank ichimill IoT Service. (2021). https://www.softbank.jp/biz/iot/service/ichimill/

Song, C., & Woodcock, C. E. (2003). Monitoring Forest Succession with Multitemporal Landsat Images: Factors of Uncertainty. *IEEE Transactions on Geoscience and Remote Sensing*, *41*(11 PART I), 2557–2567. https://doi.org/10.1109/TGRS.2003.818367

Story, M., & Congalton, R. G. (1986). Remote Sensing Brief Accuracy Assessment: A User's Perspective. *Photogrammetric Engineering and Remote Sensing*, *52*(3), 397–399. https://www.asprs.org/wp-content/uploads/pers/1986journal/mar/1986_mar_397-399.pdf

Suo, McGovern, & Gilmer. (2019). Coastal Dune Vegetation Mapping Using a Multispectral Sensor Mounted on an UAS. *Remote Sensing*, *11*(15), 1814. https://doi.org/10.3390/rs11151814

Thompson, I., Mackey, B., Mcnulty, S. G., & Mosseler, A. (2009). Forest Resilience, Biodiversity, and Climate Change. A Synthesis of the Biodiversity/Resilience/Stability Relationship in Forest Ecosystems. In *Secretariat of the Convention on Biological Diversity*. Secretariat of the Convention on Biological Diversity.

Tsai, F., Lin, T.-H., Chen, L.-C., & Chen, W. W. (2011). Landslide detection and monitoring using remote sensing and spatial analysis in Taiwan. In U. Michel & D. L. Civco (Eds.), *Earth Resources and Environmental Remote Sensing/GIS Applications II* (Vol. 8181, p. 81810V). SPIE. https://doi.org/10.1117/12.898189

Tsushima, T., & Saitoh, K. (2005). *Background to the windthrow by typhoon no. 18*.

Turner, M. G., Dale, V. H., & Everham, E. H. (1997). Fires, Hurricanes, and Volcanoes: Comparing Large Disturbances. *BioScience*, *47*(11), 758–768. https://doi.org/10.2307/1313098

Van Westen, C. (2000). Remote sensing for natural disaster management. *International Archives of the Photogrammetry, Remote Sensing and Spatial Information Sciences - ISPRS Archives*, *33*.

Vanamburg, L. K., Trlica, M. J., Hoffer, R. M., & Weltz, M. A. (2006). Ground based digital imagery for grassland biomass estimation. *International Journal of Remote Sensing*, *27*(5), 939–950. https://doi.org/10.1080/01431160500114789

Veblen, T. T., Kitzberger, T., & Lara, A. (1992). Disturbance and forest dynamics along a transect from Andean rain forest to Patagonian shrubland. *Journal of Vegetation Science*, *3*(4), 507–520. https://doi.org/10.2307/3235807

Vítková, L., Bače, R., Kjučukov, P., & Svoboda, M. (2018). Deadwood management in Central European forests: Key considerations for practical implementation. *Forest Ecology and Management*, *429*(July), 394–405. https://doi.org/10.1016/j.foreco.2018.07.034

Waldron, K., Ruel, J.-C., & Gauthier, S. (2013). Forest structural attributes after windthrow and consequences of salvage logging. *Forest Ecology and Management*, *289*, 28–37. https://doi.org/10.1016/j.foreco.2012.10.006

Walker, L. R., Zarin, D. J., Fetcher, N., Myster, R. W., & Johnson, A. H. (1996). Ecosystem Development and Plant Succession on Landslides in the Caribbean. *Biotropica*, *28*(4), 566. https://doi.org/10.2307/2389097

Wang, D., Wu, X., & Lin, D. (2009). Particle swarm mixel decomposition for remote sensing images. *2009 IEEE International Conference on Automation and Logistics*, 212–216. https://doi.org/10.1109/ICAL.2009.5262925

Wang, J., Sheng, Z., & Yu, H. (2014). Popularization of remote sensing education and general course construction in undergraduate education. *IOP Conference Series: Earth and Environmental Science*, *17*, 012262. https://doi.org/10.1088/1755-1315/17/1/012262

West, H., Quinn, N., & Horswell, M. (2019). Remote sensing for drought monitoring & impact assessment: Progress, past challenges and future opportunities. *Remote Sensing of Environment*, *232*(November 2018), 111291. https://doi.org/10.1016/j.rse.2019.111291

Woodcock, C. E., & Strahler, A. H. (1987). The factor of scale in remote sensing. *Remote Sensing of Environment*, *21*(3), 311–332. https://doi.org/10.1016/0034-4257(87)90015-0

Wu, C., Du, B., Cui, X., & Zhang, L. (2017). A post-classification change detection method based on iterative slow feature analysis and Bayesian soft fusion. *Remote Sensing of Environment*, *199*, 241–255. https://doi.org/10.1016/j.rse.2017.07.009

Wu, X., Xiao, Q., Wen, J., You, D., & Hueni, A. (2019). Advances in quantitative remote sensing product validation: Overview and current status. *Earth-Science Reviews*, *196*, 102875. https://doi.org/10.1016/j.earscirev.2019.102875

Xie, Y., Sha, Z., & Yu, M. (2008). Remote sensing imagery in vegetation mapping: a review. *Journal of Plant Ecology*, *1*(1), 9–23. https://doi.org/10.1093/jpe/rtm005

Xiong, S., & Nilsson, C. (1999). The effects of plant litter on vegetation: a meta-analysis. *Journal of Ecology*, *87*(6), 984–994. https://doi.org/10.1046/j.1365-2745.1999.00414.x

Yamamoto, S.-I. (1989). Gap dynamics in climaxFagus crenata forests. *The Botanical Magazine Tokyo*, *102*(1), 93–114. https://doi.org/10.1007/BF02488116

Zhang, S., & Wang, F. (2019). Three-dimensional seismic slope stability assessment with the application of Scoops3D and GIS: a case study in Atsuma, Hokkaido.

Geoenvironmental Disasters, *6*(1), 9. https://doi.org/10.1186/s40677-019-0125-9